energies

MDPI

Article

Investigation of Ammonia-Coal Co-Combustion Performance and NO_x Formation Mechanisms Under Varied Ammonia Injection Strategies

Yuhang Xiao [1], Jie Cui [1,*], Honggang Pan [1], Liang Zhu [2], Benchuan Xu [2], Xiu Yang [1], Honglei Zhao [1], Shuo Yang [1], Yan Zhao [1], Manfred Wirsum [3] and Youning Xu [1,*]

[1] Key Laboratory of Liaoning Province for Clean Combustion Power Generation and Heating Supply Technology, Shenyang Institute of Engineering, Shenyang 110136, China; 12023101108@stu.sie.edu.cn (Y.X.); phg666@163.com (H.P.); yangxiu779@gmail.com (X.Y.); 12021101122@stu.sie.edu.cn (H.Z.); ys_yang_shuo@163.com (S.Y.); zhaoyan223916@163.com (Y.Z.)

[2] Xinjiang Saier Shan Municipal Engineering Co., Ltd., Tacheng 839099, China; 18799239579@163.com (L.Z.); xbc18799236888@163.com (B.X.)

[3] Institute of Power Plant Technology, Steam and Gas Turbines, RWTH Aachen University, 52074 Aachen, Germany; wirsum@ikdg.rwth-aachen.de

* Correspondence: jie.cui@rwth-aachen.de (J.C.); xuyn@sie.edu.cn (Y.X.)

Abstract

In the context of carbon neutrality, ammonia-coal co-firing is considered an effective way to reduce emissions from coal-fired units. This paper takes a 125 MW tangential combustion boiler as the research object and combines CFD and CHEMKIN models to study the effects of ammonia injection position (L1–L3) and blending ratio (0–30%) on combustion characteristics and NO generation. The results indicate that L1 (same-layer premixed injection) can form a continuous and stable flame structure and maintain low NO emissions. L2 (fuel-staged configuration) shows the highest burnout rate and strong denitration potential under high mixing conditions, while L3 has an unstable flow field and the worst combustion structure. NO emissions show a typical "first rise and then fall" trend with the blending ratio. L1 performs optimally in the range of 15–20%, and L2 peaks at 20%. Mechanism analysis indicates that R430 is the main NO generation reaction, while R15 and R427 dominate the NO reduction process. The synergistic reaction between NH_x free radicals and coke can effectively inhibit the formation of NO and improve combustion efficiency.

Keywords: ammonia–coal co-firing; ammonia injection location; ammonia co-firing ratio; NO_x emissions; reaction mechanism

check for updates

Academic Editor: Roberto Finesso

Received: 17 September 2025
Revised: 18 October 2025
Accepted: 22 October 2025
Published: 25 October 2025

Citation: Xiao, Y.; Cui, J.; Pan, H.; Zhu, L.; Xu, B.; Yang, X.; Zhao, H.; Yang, S.; Zhao, Y.; Wirsum, M.; et al. Investigation of Ammonia-Coal Co-Combustion Performance and NO_x Formation Mechanisms Under Varied Ammonia Injection Strategies. *Energies* **2025**, *18*, 5609. https://doi.org/10.3390/en18215609

Copyright: © 2025 by the authors. Licensee MDPI, Basel, Switzerland. This article is an open access article distributed under the terms and conditions of the Creative Commons Attribution (CC BY) license (https://creativecommons.org/licenses/by/4.0/).

1. Introduction

To mitigate global warming caused by greenhouse gas emissions, achieving carbon peaking and carbon neutrality has become a global consensus. Countries have developed emission reduction strategies according to their respective energy structures and development stages [1]. Coal-fired power plants, as major sources of carbon emissions, can effectively reduce CO_2 output by co-firing zero-carbon fuels, providing a practical pathway toward low-carbon power generation. Among various alternatives, ammonia has attracted growing attention as a promising zero-carbon fuel because it produces no carbon dioxide during combustion. Its main combustion products are nitrogen and water vapor. In addition, ammonia offers high energy density, relatively low production cost,

and convenient storage and transportation. Therefore, ammonia–coal co-firing technology has become one of the key approaches for promoting the low-carbon transition of existing coal-fired units and has emerged as a research hotspot worldwide.

Despite its carbon-free advantage, ammonia still faces several combustion challenges: (1) poor flame stability due to its high ignition temperature and low flame propagation speed [2]; (2) high nitrogen content that promotes the formation of NO and N_2O at high temperatures, increasing NO_x emissions [3]; and (3) inhibition of CO oxidation, which reduces combustion efficiency [4]. To address these challenges, studying the combustion characteristics and pollutant formation behavior of ammonia–coal co-firing in industrial boilers is of great engineering importance. However, most existing studies focus on laboratory-scale ammonia combustion experiments, while research on numerical simulation of ammonia–coal co-firing in utility-scale boilers remains limited. Therefore, a systematic investigation of combustion behavior and NO_x emission characteristics under real furnace conditions is still urgently needed.

Currently, in terms of experiments, Masato Tamura et al. studied the center injection of the lance, the mixed injection of the coal nozzle [5], and the side wall injection of the furnace in a 1.2 MW coal-fired furnace. They found that when ammonia was injected from the coal nozzle or the lance position and the mixing ratio did not exceed 30%, the NO_x emission level was equivalent to that of pure coal combustion, while the side wall injection caused an increase in NO_x due to insufficient residence time in the reduction zone. In addition, the newly designed ammonia spray gun is able to maintain a stable flame and significantly reduce unburned carbon content under pure ammonia combustion conditions. Sung-Jin Pak et al. conducted an ammonia-coal co-combustion experiment in a pilot-scale circulating fluidized bed combustion (CFB) system [6]. By changing the NH_3 injection position and fuel classification strategy, they examined the impact of different ammonia delivery methods on NO, N_2O, CO_2 emissions, combustion efficiency, and temperature field. Tan et al. and Mathaba, respectively, found that staged combustion in tube furnaces can effectively suppress NO_x emissions produced by coal char and ammonia fuel [7,8] and concluded that ammonia-incorporated combustion can reduce unburned carbon in the ash and increase the burnout rate at all temperatures.

Compared with experimental progress, the research on numerical simulation of ammonia-coal co-combustion is relatively slow. In engineering-scale simulation research, two methods, global reaction mechanism and simplified reaction mechanism, are usually used [9]. Among them, the three-step global reaction equation commonly used in domestic and foreign research is used to describe the pyrolysis, oxidation, and reduction processes of ammonia. This modeling method with the total package reaction as the core has the advantages of high numerical stability, a wide application range, and a small calculation amount. Current mainstream research tends to use global mechanisms to solve flow fields and combustion characteristics in CFD simulations, and then combine detailed mechanisms to conduct in-depth analysis of nitrogen reaction paths and sensitivity, thereby achieving multi-scale coupling of macroscopic flow behavior and microscopic reaction mechanisms. In terms of numerical calculation of NO_x, research usually uses two types of methods: the mechanism coupling method and the post-processing method [10]. Among them, the post-processing method has become the most commonly used NO_x calculation method in engineering applications because it can significantly reduce the computational burden and maintain good consistency with experimental data in prediction results. Sousa Cardoso and others constructed a two-dimensional Euler-Lagrangian numerical model for a pilot fluidized bed and used a post-processing model to analyze NO_x [11]. They found that circulating ammonia under the fluidized bed will lead to higher NO emissions, and only 20% air classification can reduce NO emissions by 50%. Liu et al. conducted a numerical

simulation study on an ammonia-coal mixed combustion burner [12]. In the model, three total package reactions of ammonia's pyrolysis, oxidation, and reduction were used to represent the main reaction process of ammonia, and the generation of nitrogen oxides was predicted and analyzed through a post-processing NO_x model. The results show that when the ammonia doping ratio is 10%, the ammonia oxidation reaction dominates and NO emissions increase significantly. As the ammonia doping ratio increases to 20–30%, the flame changes from a swirling flame to a slender flame. NH_3 oxidation is limited, pyrolysis is enhanced, and NO emissions are significantly reduced. When the ammonia doping ratio is further increased to 50%, mixing is intensified, oxidation is intensified, and NO emissions increase again.

On the basis of understanding the ammonia combustion mechanism and NO_x generation rules, researchers began to pay attention to the impact of operating parameters such as ammonia injection methods and blending ratios on combustion and emission characteristics. Wang et al. conducted an analysis of ammonia-coal mixed combustion characteristics using a 600 MW supercritical boiler as the research object [13]. The results showed that NO_x emissions first increased and then decreased with the increase in ammonia mixing ratio. When the ammonia mixing ratio was 10%, the NO_x concentration reached a peak. In addition, the ammonia burner arranged at a high position produces a higher NO_x concentration than a low-position burner, but at the same time, it can effectively reduce the carbon content of fly ash, thereby improving combustion efficiency. Ma studied the ammonia gas inlet position of a 20 kW settling furnace through numerical simulation and found that the greater the distance between the ammonia injection position and the pulverized coal flame zone [14], the higher the carbon content and NO concentration of the fly ash. Jin et al. conducted a numerical simulation study on the impact of ammonia doping ratio on a 1050 MW coal-fired boiler [15]. The results showed that as the ammonia doping ratio increases, the furnace temperature gradually decreases, CO_2 emissions drop to about 20% of pure coal combustion, while H_2O emissions increase by about 4 times. At the same time, the study found that the oxidation reaction of ammonia is more significant than the reduction reaction and plays a dominant role in the overall combustion process. Seong-Ju Kim et al. took a circulating fluidized bed device as the research object and explored the effects of combustion characteristics and pollutant emissions in the furnace at three ammonia flow positions [16], upper, middle, and lower, based on a fixed ammonia doping ratio of 25%. A comprehensive analysis concluded that spraying ammonia at a medium speed in the lower or middle area of the furnace can effectively control NO emissions while ensuring combustion stability.

Overall, although some progress has been made in the study of ammonia–coal co-firing, most existing work still focuses on small-scale or pilot-scale experimental setups, while numerical simulations for tangentially fired boilers remain limited. In this study, a 125 MW tangentially fired coal-fired boiler was selected as the research object to systematically compare the combustion and emission characteristics under three typical ammonia injection configurations and various blending ratios. Considering the current structure and operating conditions of industrial boilers, an excessively high ammonia fraction can cause combustion instability, temperature field distortion, and convergence difficulties in numerical simulations [17]. Moreover, such high blending ratios currently lack engineering feasibility and economic justification. Therefore, the ammonia blending ratio in this study was limited to 0–30% to ensure that the simulation results are representative and that the model remains both stable and comparable across cases. The Fluent-based CFD simulations were used to reveal the effects of ammonia injection modes on the temperature and NO_x distributions, while Chemkin-based kinetic modeling under the same fuel and air conditions was employed to identify the key reaction pathways of the ammonia combustion

process. This study integrates macroscopic CFD results with microscopic kinetic analysis, providing theoretical support for optimizing low-NO_x combustion in large-scale boilers and promoting the practical application of ammonia-based zero-carbon fuels.

2. Boiler Model and Mesh Generation

The 125 MW tangentially fired, once-through boiler model used in this study is shown in Figure 1. The reference unit, located in Jilin City, Jilin Province, China, is a single-drum, vertical water-tube, natural-circulation, sealed-membrane, water-cooled wall boiler with the model designation E-360-13.8-560KBT. Its external dimensions are 8.70 m in width, 8.65 m in depth, and 34.70 m in height.

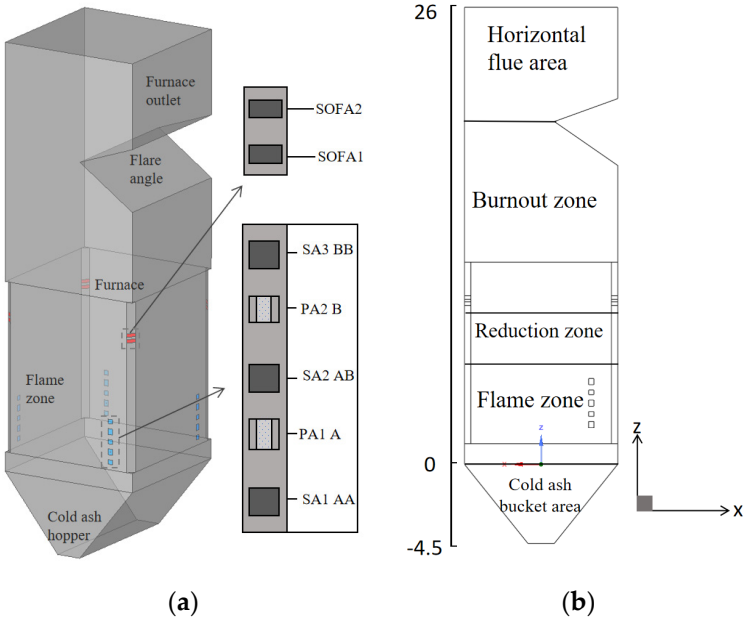

Figure 1. Boiler model (**a**) schematic diagram of boiler structure; (**b**) division of different areas of boiler.

The furnace features a tangentially fired burner arrangement with uniform air distribution, utilizing once-through burners with a tangential circle diameter of 0.65 m. The combustion air system is composed of two layers containing a total of eight primary air nozzles, three layers with twelve secondary air nozzles, and two layers with eight separated overfire air (SOFA) nozzles. To optimize in-furnace combustion conditions, improve combustion efficiency, and reduce the flue gas temperature gradient, the secondary air in the AB layers is arranged in a reverse-tangential configuration while maintaining the same tangential circle diameter of 0.65 m.

The furnace is divided into four functional zones: the cold ash hopper zone (−4.5 to 0 m), the main combustion zone (0 to 5 m), the reduction zone (5 to 9 m), and the burnout zone (9 to 14 m). Since the primary chemical reactions occur mainly in the main combustion, reduction, and burnout zones, this study focuses on these three regions for detailed investigation.

The boiler model was meshed using ANSYS ICEM CFD (Version 2021 R1), as shown in Figure 2a, with local mesh refinement applied in critical regions such as burner outlets. To verify mesh independence, three sets of unstructured mesh systems with different cell counts—1,094,188, 1,437,360, and 1,708,712—were generated. Mesh independence validation was conducted by comparing the average temperature distribution, NO concentration, and CO_2 mole fraction along various cross-sections in the furnace height direction, as illustrated in Figure 2b.

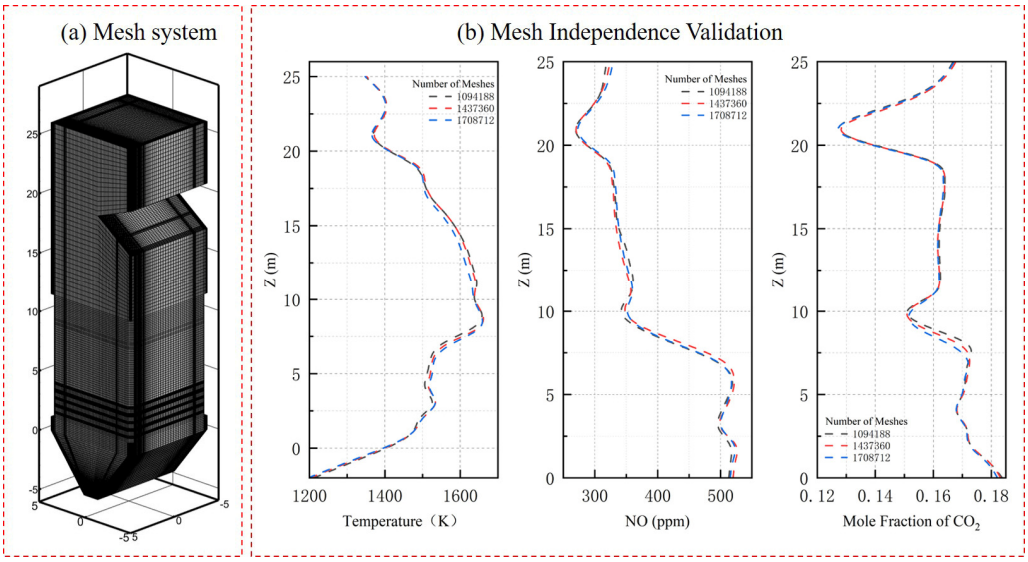

Figure 2. Boiler model and grid independence verification (**a**) boiler meshing; (**b**) verification of mesh independence of temperature and gas components.

The results indicate that increasing the mesh count from 1.09 million to 1.43 million significantly reduced differences in curve shape, gradient, and peak position, while further increasing it to 1.70 million yielded only marginal improvements. Therefore, considering both computational accuracy and cost, the medium-scale mesh with 1,437,360 cells was selected for subsequent simulations, ensuring reliable results while substantially reducing computational resource consumption.

The fuel used in this study is bituminous coal, with its proximate and ultimate analyses presented in Table 1. The pulverized coal particle size distribution follows the Rosin–Rammler model, featuring a maximum diameter of 250 μm, a minimum diameter of 10 μm, an average diameter of 50 μm, a distribution modulus of 1.15, and a total of 10 particle size classes.

Table 1. Properties of fuels.

Proximate Analysis (wt.%, ar)				Ultimate Analysis (wt.%, ar)					Low Heating Value /(MJ/kg)
M	**V**	**FC**	**A**	**C**	**H**	**O**	**N**	**S**	
14.5	21.24	39.77	10.33	58.54	3.48	11.90	0.79	0.44	23.28

For the numerical simulations, the boundary conditions were specified as follows: the turbulence intensity at the primary air, secondary air, and overfire air (OFA) inlets was set to 10%. The initial furnace wall temperature was defined as 690 K, with the bottom furnace temperature at 473 K. The boiler outlet was assigned a pressure outlet boundary condition with a static pressure of −20 Pa and a temperature of 1000 K. For the discrete phase, the injection temperature of pulverized coal particles was set to 338 K, consistent with the primary air temperature. The injection temperatures for the secondary air and OFA were set to 601 K. At the outlet boundary, the Discrete Phase Model (DPM) condition was set to escape, while the primary air, secondary air, and OFA inlets were set to reflect, and the cold ash hopper zone was set to trap. The excess air ratio for furnace combustion was set to 1.15. Other parameters, including coal feed rate and primary and secondary air velocities, were either directly specified or calculated based on the actual operational parameters of the boiler, as summarized in Table 2.

Table 2. Air distribution parameters of pure coal-fired conditions.

Wind Gap	Air Rate (%)	Temperature (K)	Velocity (m/s)
Primary air	26	338	25.82
Secondary air	37	601	30.68
Overfire air	37	601	30.68

3. Numerical Simulation

3.1. Model Description and Validation

In this study, the pulverized coal–ammonia co-firing process in a boiler was numerically simulated using ANSYS Fluent (Version 2021 R1). This process involves a complex coupling of multiple physical phenomena, including gas-phase turbulence, particle motion, devolatilization and combustion, radiative heat transfer, and pollutant formation. Pulverized coal combustion consists of devolatilization and combustion of volatiles, as well as char oxidation. The introduction of ammonia adds additional pyrolysis, intermediate reactions, and coupling effects with coal combustion, thereby increasing the model's complexity.

To balance computational accuracy with engineering applicability, the Reynolds-Averaged Navier–Stokes (RANS) approach was employed as the computational framework. The gas–solid two-phase interaction was resolved using the Euler–Lagrange method: the continuous phase was solved using the Eulerian equations, while coal particle trajectories were tracked with the Discrete Phase Model (DPM) [18]. Turbulence was modeled using the standard k–ε model combined with wall functions, and radiative heat transfer was computed using the P-1 model in conjunction with the Weighted Sum of Gray Gases Model (WSGGM) to account for the spectral properties of CO_2 and H_2O [19–21]. Chemical reactions were modeled using the finite-rate/eddy dissipation model (EDM) to describe the turbulent–chemistry interactions of NH_3 pyrolysis products, coal volatiles, and gas-phase intermediates. Char oxidation was represented by a multi-surface reaction scheme based on the Langmuir–Hinshelwood mechanism [22], incorporating heterogeneous reaction pathways involving O_2, CO_2, and H_2O.

NO_x emissions were calculated during a post-processing stage. Since no unified reaction mechanism currently exists for ammonia–coal co-firing, a combined approach addressing both thermal NO_x and fuel NO_x was employed, based on engineering boiler and pilot-scale experimental studies [23–25]. The contribution of prompt NO_x was neglected, as it accounts for less than 5% [26]. Fuel NO_x was identified as the dominant source, contributing more than 80% of the total NO_x emissions, and was primarily formed through the volatilization and oxidation of nitrogen species during coal and ammonia combustion. The relevant fuel NO_x formation pathways and key reaction parameters are presented in Figure 3 and Table 3.

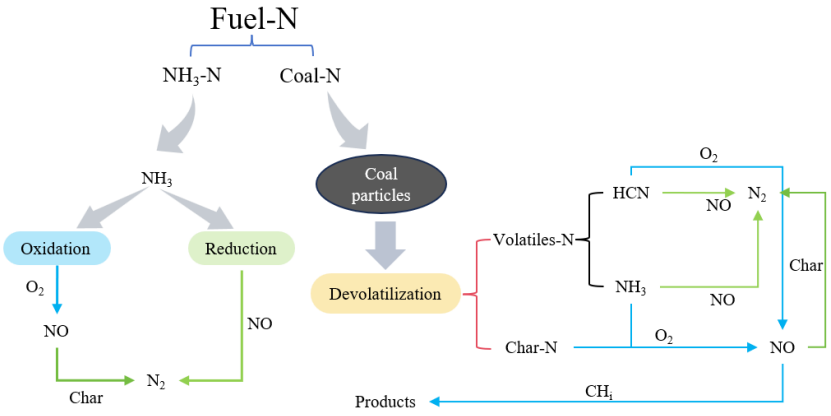

Figure 3. Reaction path of nitrogen element in ammonia coal co-combustion process.

Table 3. Global mechanism and kinetic parameters.

Chemical Equation	A/(s^{-1})	Ea/(J/kmol)	R-e	Reference
Coal combustion				
$R_1.vol + 0.878O_2 \rightarrow 0.775CO + 1.6781H_2O + 0.0274N_2$	2.119×10^{11}	2.027×10^{8}	$[vol]^{0.2}[O_2]^{1.3}$	
$R_2.C + 0.5O_2 \leftrightarrow CO$	0.00500	7.369×10^{7}		[27]
$R_3.C + H_2O \rightarrow CO + H_2$	0.00192	1.469×10^{8}		[28]
$R_4.C + CO_2 \rightarrow 2CO$	0.00635	1.62×10^{8}		[28]
$R_5.H_2 + 0.5O_2 \leftrightarrow H_2O$	5.69×10^{11}	1.47×10^{8}	$[H_2][O_2]^{0.5}$	[29]
$R_6.CO + H_2O \leftrightarrow CO_2 + H_2$	2.75×10^{9}	8.36×10^{7}	$[CO][H_2O]$	[30]
$R_7.CO + 0.5O_2 \rightarrow CO_2$	1.93×10^{13}	1.26×10^{8}	$[CO][O_2]^{0.25}$	[31]
Ammonia Pyrolysis Oxidation				
$R_8.NH_3 \rightarrow 0.5N_2 + 1.5H_2$	0.18500	6.90×10^{7}	$[NH_3]$	[32]
$R_9.NH_3 + O_2 \rightarrow NO + H_2O + 0.5H_2$	3.5×10^{2}	5.24×10^{8}	$[NH_3][O_2]$	[33]
$R_{10}.NH_3 + NO \rightarrow N_2 + H_2O + 0.5H_2$	4.24×10^{5}	3.50×10^{8}	$[NH_3][NO]$	[33]

To validate the accuracy of the numerical model, Figure 4 presents a comparison between the Fluent simulation results and the actual operational measurements of the power plant boiler under pure coal combustion conditions. The comparison focuses on flue gas temperature, NO_x concentration, and oxygen content at the boiler horizontal flue outlet. The simulated flue gas temperature was 1126.45 K, compared with a measured value of 1142.71 K, resulting in a relative error of 1.44%. The simulated NO_x concentration was 333.8 ppm, while the measured value was 328.5 ppm, with the error remaining within 2%. The simulated oxygen content at the outlet was 1.94%, compared to a measured value of 2.01%, indicating minimal deviation.

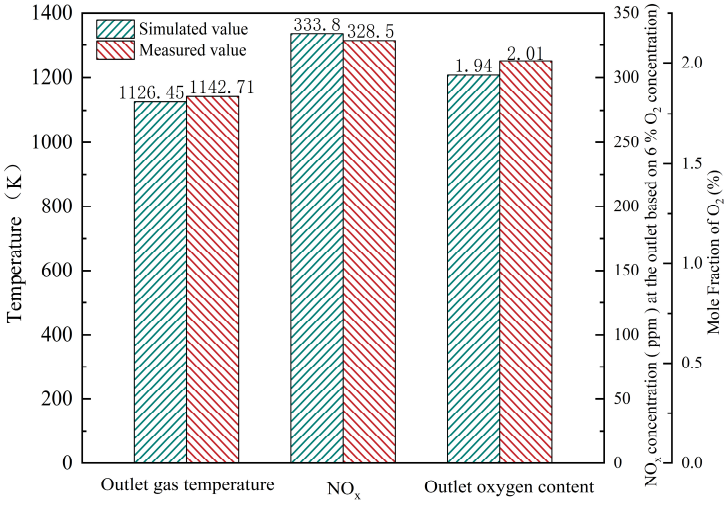

Figure 4. Comparison of temperature, NO_x, and oxygen concentration at furnace outlet under pure coal conditions.

These results demonstrate that the developed numerical model accurately predicts the temperature field and major pollutant emissions. The close agreement between simulated and measured values confirms that the model reliably captures the combustion process inside the furnace. Therefore, it provides a robust foundation for the subsequent ammonia–coal co-firing simulations in this study, offering dependable engineering applicability and valuable reference data.

3.2. Ammonia–Coal Reaction Mechanism

To enhance the computational efficiency of the numerical simulations, appropriate simplifications were applied to the modeling of the boiler combustion process. Pulverized

coal was assumed to undergo instantaneous devolatilization upon injection into the furnace, with the released volatiles treated as being in thermodynamic equilibrium and used as the initial conditions for chemical kinetic calculations. The pyrolysis products were assumed to be perfectly mixed with the oxidizer, while the effects of ash and gas-phase heating were neglected, allowing the internal reactions in the boiler to be approximated as an ideal one-dimensional continuous flow system. Based on the structural segmentation of the boiler and the characteristics of air staging, a simplified reactor network model was developed on the CHEMKIN (Version 2021 R1) platform, as shown in Figure 5. This model integrates Perfectly Stirred Reactors (PSRs) and Plug Flow Reactors (PFRs) to represent the combustion processes in different functional regions. Specifically, two PSRs (C1_R1 and C1_R2) in series were employed to simulate the primary air–coal combustion process and the subsequent reactions following secondary air injection in the main combustion zone; a single PSR (C1_R3) was used to describe local reburning effects induced by high-temperature flue gas recirculation; the burnout zone was modeled by a PSR (C1_R4) to account for the deep oxidation between overfire air and incompletely reacted species; the horizontal flue was represented by a PSR (C1_R5) to capture the final compositional changes before the outlet; and the downstream recirculation and tail flue gas passage were approximated by a PSR (C1_R6) and a PFR (C2), respectively, to simulate the flow and heat transfer processes in the rear section.

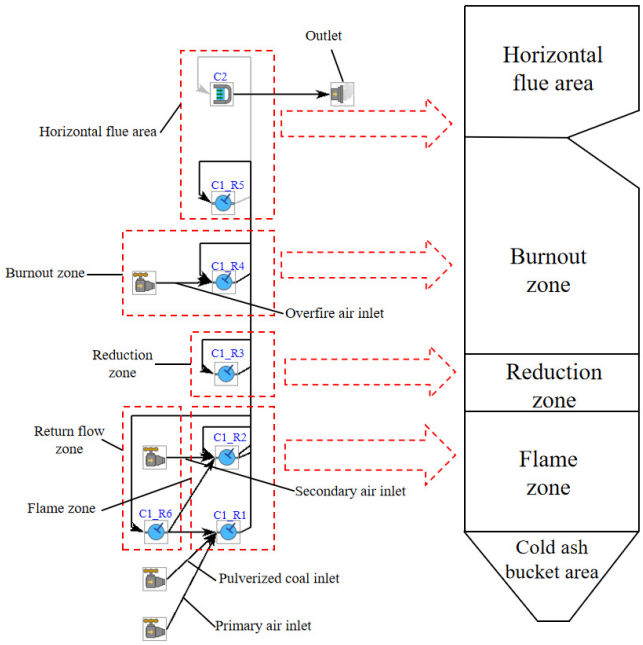

Figure 5. Reaction network model diagram.

In this study, the detailed chemical kinetic mechanism proposed by Hashemi et al. was employed [34]. This mechanism involves five elements—C, H, O, N, and Ar—and includes key reactants and products such as NH_3, NH_2, NH, NO, and N_2O. It comprehensively accounts for ammonia pyrolysis, oxidation, and the formation and reduction pathways of NO under high-temperature conditions. The mechanism comprises 768 elementary reactions, covering multiple reaction types, including char oxidation, soot formation, and volatile oxidation, thereby providing high adaptability and completeness. It has been widely applied to simulate high-temperature combustion processes involving ammonia-based fuels. However, such detailed mechanisms typically adopt simplified volatile matter models to represent coal pyrolysis, in which volatile components are generally defined as light gaseous species such as CO, H_2, H_2O, CH_4, C_2H_4, and C_2H_6 [35–37]. This simplification

fails to capture the differences in molecular structure, aromaticity, and nitrogen content among various coal types, thereby limiting the ability to accurately reflect the influence of coal properties on actual combustion behavior and pollutant formation pathways.

To address this limitation, the FLASHCHAIN macromolecular pyrolysis model was developed [38]. This model incorporates a four-step reaction pathway and a statistical description of molecular chain segments. Based on fundamental physicochemical properties-such as the ultimate analysis of coal (Table 1) and aromaticity parameters (e.g., aromatic carbon fraction f_a and aromatic cluster size)-FLASHCHAIN constructs the distribution of structural units within the coal matrix and predicts the release of primary and secondary products under high-temperature pyrolysis conditions. Considering its applicability in subsequent detailed chemical kinetic simulations, this study adopted the species categorization scheme reported by Ishihara et al. and recalibrated the mass fractions based on the actual composition of the coal used in this work [39], ensuring a closer representation of the real volatile composition. The mass composition of coal (char + volatiles) used as input data is provided in Table 4.

Table 4. Input coal quality composition data (Coke + Volatile).

Components of Coal	Mass Fraction of Coal
Char ($C_{412}N_5$)	0.41554
Soot (C_{166})	0.54613
CH_4	0.00106
C_2H_2	0.00782
H_2	0.00862
CO	0.00641
CO_2	0.00261
H_2O	0.00381
HCN	0.00541
NH_3	0.00038
N_2	0.00221
Toal	1

To ensure thermochemical and operational consistency between the Fluent and CHEMKIN models, the reactor network inputs were quantitatively determined based on the CFD results. Specifically, each reactor in the CHEMKIN model corresponds to a representative combustion zone in the CFD domain, as summarized in Table 5. In addition, key operating parameters such as the pulverized coal feed rate, NH_3 injection flow rate, primary and secondary air temperatures, excess air coefficient, and air distribution ratio were set according to the boundary conditions in the CFD model to maintain thermodynamic consistency across the two platforms.

Table 5. Mapping relationship between CFD combustion zones and CHEMKIN reactors with corresponding operating parameters.

Reactor NO.	Corresponding CFD Zone	Pulverized Coal Feed Rate (kg/s)	NH_3 Injection Flow Rate (m^3/s)	Primary Air Temperature (K)	Secondary and Overfire Air Temperature (K)	Excess Air Coefficient	Air Distribution Ratio (Primary: Secondary: Overfire)
Reactor 1,2,6	Main combustion zone	10.0725	2.935	338	601	1.15	26:37:37
Reactor 3	Reduction Zone	-	-	-	-	-	-
Reactor 4,5	Burnout zone	-	-	-	601	1.15	26:37:37

4. Discussion

4.1. Effect of Ammonia Injection Location on Combustion Characteristics and NO_x Emissions

Previous studies have demonstrated that the injection location of ammonia within the furnace significantly impacts the combustion process and pollutant emissions [40–42]. Considering that some boilers face structural constraints and high retrofit costs in practical engineering applications, this study retains the original furnace geometry and introduces ammonia solely through the existing primary air (PA) ports. The ammonia co-firing ratio was set at 15%, with the air distribution among the primary air, secondary air, and overfire air (OFA) ports maintained at 26%, 37%, and 37%, respectively. Given the limited number of PA ports in the selected boiler configuration, three ammonia injection schemes were designed based on the existing burner arrangement: (1) Ammonia was premixed with pulverized coal and jointly delivered into the furnace via the PA ports, with the ammonia temperature identical to that of the primary air, corresponding to Case L1; (2) Ammonia was injected through the bottom-layer PA ports, while pulverized coal was injected through the top-layer PA ports, corresponding to Case L2; (3) Pulverized coal was injected through the bottom-layer PA ports, while ammonia was injected through the top-layer PA ports, corresponding to Case L3. The specific configurations and burner arrangements for each case are presented in Table 6 and Figure 6.

Table 6. Ammonia injection position setting conditions.

Load	Ammonia Injection Location	Ammonia Blending Ratio (%)
L1	pa1, pa2	15
L2	pa1	15
L3	pa2	15

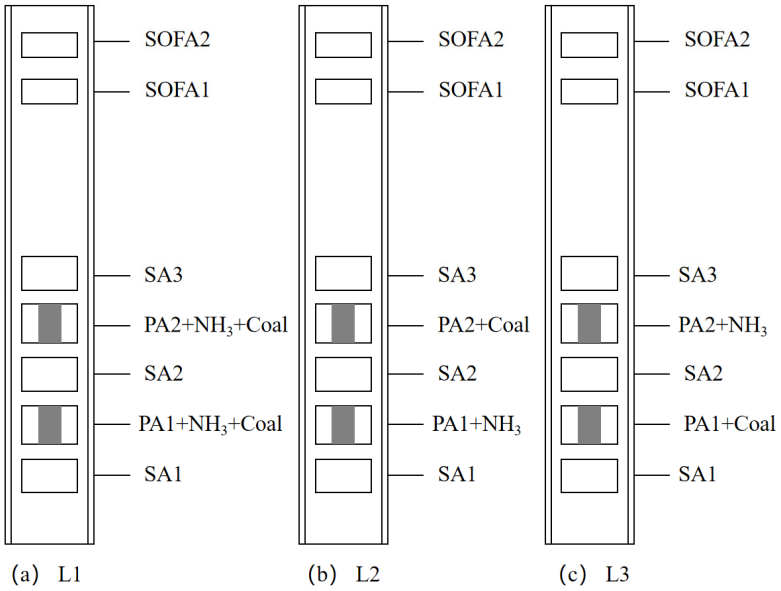

Figure 6. Schematic diagram of the layout of different ammonia ventilation positions (**a**) L1—Ammonia–coal mixture injected through the primary air port; (**b**) L2—Coal supplied by the bottom primary air, ammonia injected through the upper secondary air; (**c**) L3—Coal supplied by the bottom primary air, ammonia injected through the top secondary air.

As shown in Figure 7, there are significant differences in the axial velocity distribution of the furnace under different ammonia flow modes. The L1 working condition forms a continuous ascending airflow channel in the main combustion zone and the reduction zone. The overall speed is mainly forward. The airflow near the nozzle is stable and

concentrated, showing the characteristics of short jet penetration and sufficient mixing, which is conducive to the uniform transport of cracked products and active gas along the axial direction and maintains flame stability. The L2 operating condition also maintains the ascending flow structure, but the ammonia injection speed is higher, and the momentum flux ratio increases, which makes the air flow penetrate deeper, the mixing is relatively delayed, the local velocity gradient increases, and the air flow distribution tends to be uneven. In contrast, the L3 operating condition has an obvious negative Z-direction velocity area in the lower part of the main combustion zone, and the air flow locally produces downward reflux and velocity reversal phenomena, resulting in a certain axial pressure difference in the furnace, destroying the overall upward flow channel, causing some combustible components to stay in the lower part, and mixing is restricted. This result shows that the flow field structure of L1 is most conducive to stable combustion and complete burnout; L2 may have local ammonia-rich areas under moderate blending and cause an increase in NO production; while L3 is more likely to cause a decrease in combustion efficiency and emission fluctuations due to turbulent airflow distribution and uneven mixing.

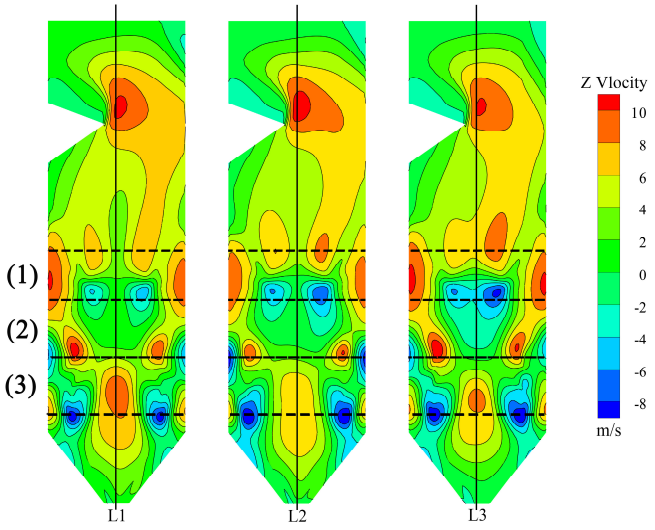

Figure 7. Z-velocity distribution inside the furnace under different ammonia injection positions (L1–L3); (1) burnout zone, (2) reduction zone, and (3) main flame zone.

To further quantify the velocity gradients and the interaction strength between the injected ammonia jet and the mainstream observed in the velocity field, the momentum-flux ratio (M) is introduced as a dimensionless indicator. This parameter characterizes the relative jet momentum with respect to the surrounding furnace flow and serves as an effective measure of jet penetration and mixing behavior. In this study, the calculation of M is based on the pure-coal baseline condition, where the average density and velocity of the mainstream at the same height as the injection nozzle are used as the reference denominator. All parameters are obtained from mass-weighted averages of Fluent simulation results under different operating conditions to ensure physical consistency. A higher M value indicates that the injected jet possesses stronger momentum relative to the main flow, leading to deeper penetration and delayed mixing, whereas a lower M corresponds to weaker jet momentum, enhanced entrainment, and a more uniform flow field. The momentum/flux ratio is calculated as follows:

$$M = \frac{\rho_j u_j^2}{\rho_{m0} u_{m0}^2} \quad (1)$$

Among them, ρ_j and u_j denote the average density and average velocity of the mixed gas at the nozzle outlet, respectively, while ρ_{m0} and u_{m0} represent the average density and average velocity of the furnace mainstream at the same height as the nozzle under pure-coal baseline conditions, which are used as the reference denominator.

It can be seen from Table 7 that L2 has the highest momentum flux ratio in the PA1 layer, and the jet flow volume is significantly stronger than the mainstream, forming a deeper penetration and backflow structure. Although it is beneficial for lower burnout, the mixing is relatively delayed. The momentum flux ratio of L1 in both layers is slightly less than 1. The jet flow is equivalent to the main flow volume, forming a uniform flow characteristic of short jets and rapid entrainment, and the overall flow field is relatively stable. In contrast, although the momentum flux ratio of L3 in the PA2 layer is only slightly higher than that of L1–PA2, the mainstream in the upper area has formed a continuous spiral upward channel, and the enhanced jet flow significantly offsets the updraft, causing the upper velocity field to be disturbed, causing backflow and velocity reversal. It can be seen that the velocity distribution of L3 is more uneven, the continuity of the ascending channel is weakened, and the overall flow field coherence and stability are lower than in other working conditions.

Table 7. Averaged velocity and density of the NH_3–air jet and the interacting main flow under different ammonia injection configurations (L1–L3).

Case	ρ_j (kg/m^3)	u_j (m/s)	ρ_{m0} (kg/m^3)	u_{m0} (m/s)	M
L1-PA1	0.23990	14.70571	0.25398	14.59870	0.958
L1-PA2	0.24035	14.54520	0.25659	14.90846	0.892
L2-PA1	0.26274	15.21872	0.25398	14.59870	1.124
L3-PA2	0.23595	15.24661	0.25659	14.90846	0.962

Figure 8 illustrates the temperature distributions within the furnace under different ammonia injection schemes. In Case L1, a concentrated and stable high-temperature core forms in the lower part of the main combustion zone, with symmetrical isotherm contours. This indicates sufficient reaction between ammonia and pulverized coal, a continuous flame structure, and favorable conditions for stable combustion. In Case L2, although the temperature in the lower region is slightly reduced, the high-temperature zone extends more broadly and uniformly along the furnace height. This reflects effective mixing between ammonia introduced from the lower layer and the descending coal particles in the mid-region, resulting in a sustained combustion process that promotes higher burnout rates. In contrast, in Case L3, the high-temperature zone is concentrated in the middle of the furnace, with significantly lower temperatures in the burnout zone. The disruption of the flame structure suggests that ammonia injected from the upper layer fails to effectively participate in reactions within the main combustion zone, leading to poorer combustion organization.

Figure 9 presents the axial distributions of temperature, O_2, CO, and CO_2 mole fractions under different ammonia injection positions. From Figure 9a, Case L3 reaches its peak temperature of approximately 1650 K at Z ≈ 6 m, indicating the strongest reaction intensity in the main combustion zone. However, the temperature decays rapidly thereafter, resulting in the lowest tail-end temperature and suggesting highly concentrated heat release with poor combustion sustainability. In contrast, Case L2 exhibits a slightly lower peak temperature but maintains an extended mid-to-late-stage temperature plateau and the highest outlet temperature, reflecting a more stable reaction structure and a more complete heat release process. Case L1 falls between the two, showing a rapid temperature rise followed by a gradual decay, indicative of moderate heat release intensity and combustion persistence. In Figure 9b, Case L2 records the lowest O_2 concentration within Z ≈ 3–5 m,

implying intense reactions and nearly complete oxygen consumption in the main combustion zone. Case L1 displays slower oxygen depletion, with more uniform but less intense reactions. Case L3 maintains relatively high oxygen levels throughout the main combustion zone; despite its high temperature, the insufficient oxygen consumption suggests poor mixing between fuel and oxidant, resulting in inferior combustion performance. As shown in Figure 9c, the CO peak near Z ≈ 2 m is highest for Case L3, indicating vigorous production of reducing gases but delayed oxidation, which increases the risk of incomplete combustion. Case L2 has a slightly lower CO peak that decreases more rapidly, indicating a closer coupling between pyrolysis and oxidation processes, thereby enhancing combustion completeness. Case L1 exhibits a relatively flat CO profile with a bimodal structure, suggesting balanced but less intense reactions. In Figure 9d, although Case L3 shows a high CO_2 peak in the main combustion zone, the concentration declines rapidly toward the tail section, yielding the lowest outlet value, which indicates localized product generation and incomplete subsequent combustion. For Case L2, CO_2 concentration continues to rise through the mid-section, reaching its maximum at the outlet, signifying good combustion continuity and sufficient product accumulation. Case L1 maintains relatively stable CO_2 generation with a more uniform spatial distribution.

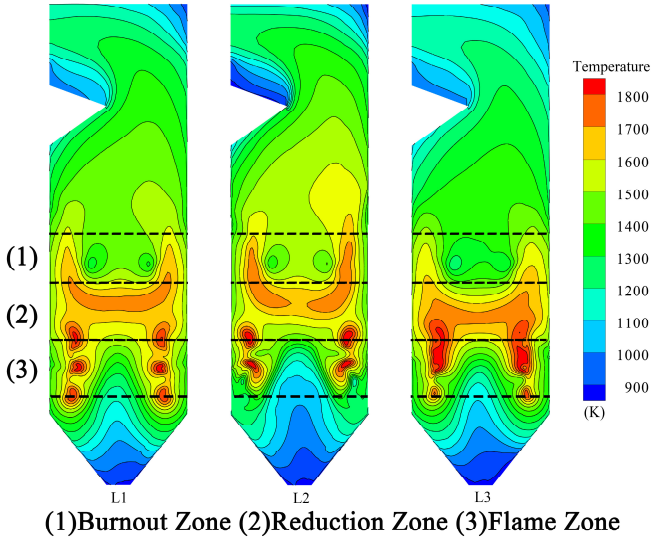

Figure 8. Temperature distribution cloud diagram inside the furnace at different ammonia injection positions (L1–L3). (1) Burnout zone, (2) Reduction zone, and (3) Main flame zone.

Figure 10 shows the distribution of burnout reaction rates of pulverized coal particles in the furnace at different ammonia flow positions (particle mass loss rate calculated based on the DPM). The results show that there are obvious differences in the spatial distribution characteristics of combustion reactions under each working condition. In the L2 operating condition, the high burnout rate area is continuously distributed from the bottom nozzle upwards, forming a through main reaction channel, indicating that the fuel is fully burned in the furnace, and the overall burnout rate reaches about 98.83%, which is the highest among the three schemes. Under the L1 working condition, the high-value areas are mainly concentrated near the primary air nozzles on the upper and lower floors. Although the local reaction intensity is high, the vertical ductility is insufficient, the combustion in the middle is weak, and the final burnout rate is about 96.23%. In contrast, the high burnout zone under L3 operating conditions is mainly distributed under the nozzle, expanding laterally but with limited vertical development. There is basically no obvious reaction zone in the middle and upper parts, resulting in an overall burnout rate of only about 90.39%. Comprehensive comparison shows that the L2 ammonia flow mode forms the

most coherent flame structure and the highest burnout efficiency, followed by L1, while the L3 airflow organization is poor, the combustion reaction distribution is discrete, and the burnout performance is the weakest.

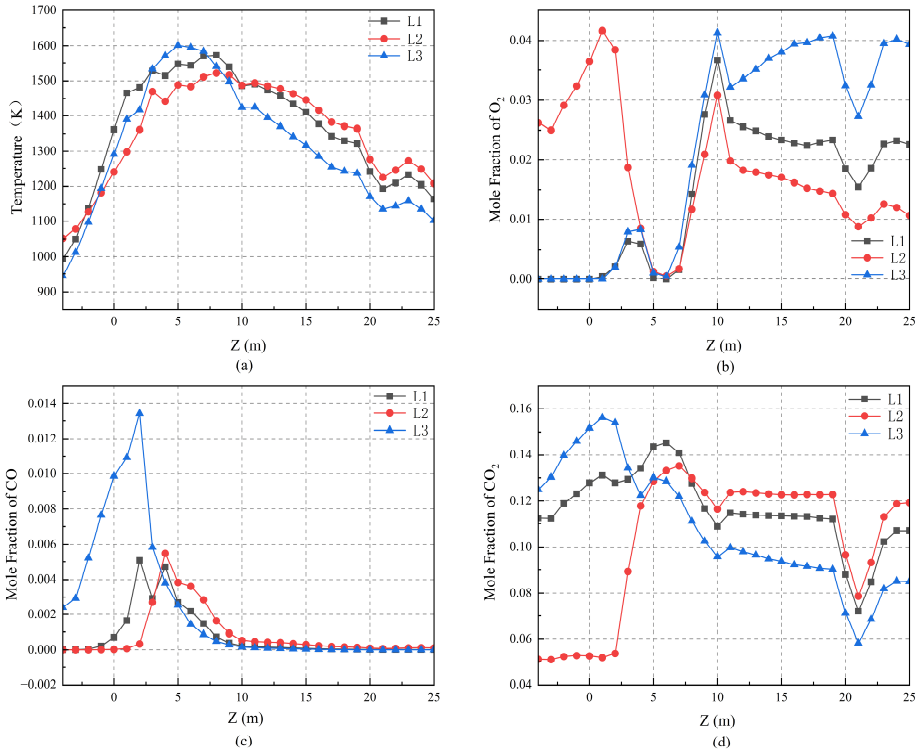

Figure 9. Distribution curves along the furnace height at different ammonia injection positions: (**a**) temperature, (**b**) O_2 concentration, (**c**) CO concentration, (**d**) CO_2 concentration.

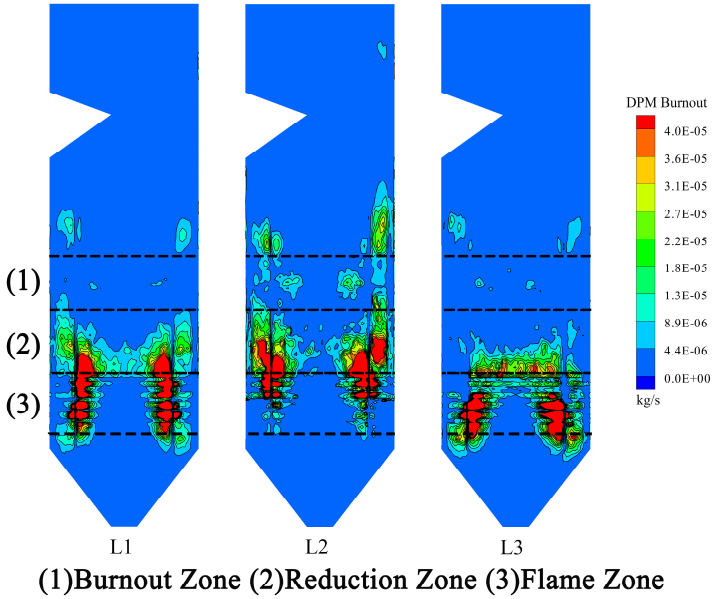

Figure 10. Combustion rate cloud diagram of pulverized coal particles at different ammonia injection positions (L1–L3). (1) Burnout zone, (2) reduction zone, and (3) main flame zone.

Figure 11a shows the NO concentration distribution curves along the height direction of the lower furnace at three ammonia passing positions. In the L2 operating condition, the highest peak appears in the main combustion zone (Z ≈ 2–5 m), indicating that the NO generation reaction is extremely violent under the conditions of full ammonia-coal

reaction and high combustion temperature. Although partial reduction occurs in the middle and later stages, overall emission levels are still in the medium to high range. In the L1 operating condition, the peak value is significantly lower than in other operating conditions, and the NO concentration curve shows a relatively gentle change trend. The uniform ammonia distribution in the main combustion zone promotes moderate reaction intensity and forms a partially reducing atmosphere, effectively inhibiting the generation and accumulation of NO. In the L3 operating condition, a large amount of NO is rapidly generated in the upper part of the main combustion zone, and the subsequent reduction efficiency is limited, resulting in the final emission concentration of this configuration being the highest among the three operating conditions. As can be seen from Figure 11b, in general, the three ammonia passing positions will produce a large amount of NO_x, among which the NO_x content at the L3 outlet is the highest. Compared with the pure coal working condition, the NO_x content increased by 491.1%, working condition L2 increased by 243.4%, and working condition L1 increased by 108.8%. Working condition L1 injects ammonia evenly through the upper and lower primary tuyere to maintain moderate temperature and oxygen consumption, promoting the generation of intermediate free radicals such as NH_2 and NH. These free radicals promote the reduction in NO, significantly reducing the overall NO level and the concentration at the furnace outlet. In the L2 operating condition, ammonia gas is injected from the bottom, causing a violent reaction between NH_3 and coal in the main combustion zone, producing a large amount of NO under high temperature and oxygen-rich conditions. Although there is a reduction reaction in the middle and late stages, the final NO emissions are still significantly higher than the L1 operating condition. In the L3 operating condition, the ammonia introduced from the upper part failed to effectively participate in the reduction reaction of NO generated in the lower area. Instead, it continued to promote the formation of NO in the high-temperature oxidizing atmosphere, resulting in the highest emissions among the three ammonia injection strategies.

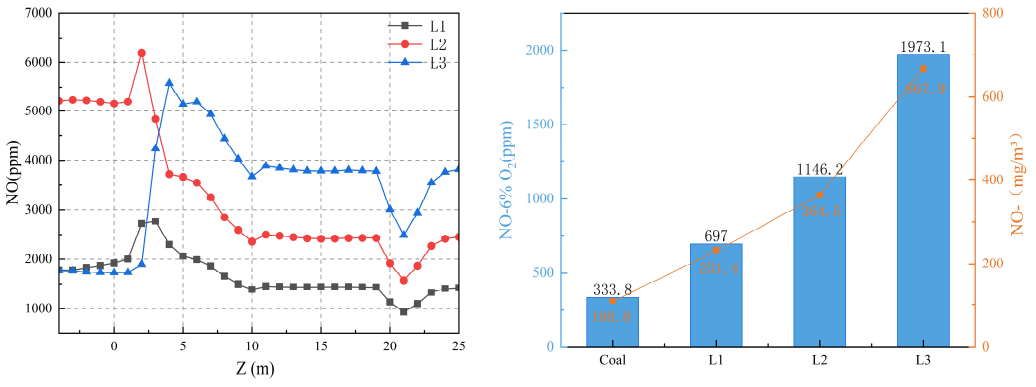

(**a**) (**b**)

Figure 11. (**a**) The NO distribution curve along the height of the furnace at different ammonia injection positions, and (**b**) the NO concentration distribution at the outlet.

Figure 12 shows the axial distributions of ammonia-involved pyrolysis and reduction reaction rates (R8, R9, R10) under the three ammonia injection configurations. In both Cases L1 and L2, the reaction rate peaks occur at Z ≈ 2 m, in the middle of the main combustion zone, indicating that ammonia can decompose promptly in high-temperature, strongly reducing regions and subsequently couple with NO through reduction reactions. Notably, in Case L2, ammonia injected from the bottom is thoroughly mixed with descending coal particles, resulting in the highest reaction intensity, the steepest rate profiles, and the most complete reaction coupling. In contrast, Case L3 exhibits significantly weakened reaction rates, with the peak shifted upward to Z ≈ 3–4 m and primarily dominated by pyrolysis.

This indicates that ammonia injected from the upper level has difficulty penetrating into the core reaction zone, leading to insufficient formation of intermediate radicals necessary for NO reduction. Combined with the previous analysis, it can be inferred that in Case L3, the upper-layer ammonia is influenced by vertical pressure differentials induced by lower-zone thermal flows, causing stagnation and dilution effects that limit the effective utilization of NH_3 and the establishment of reduction reactions.

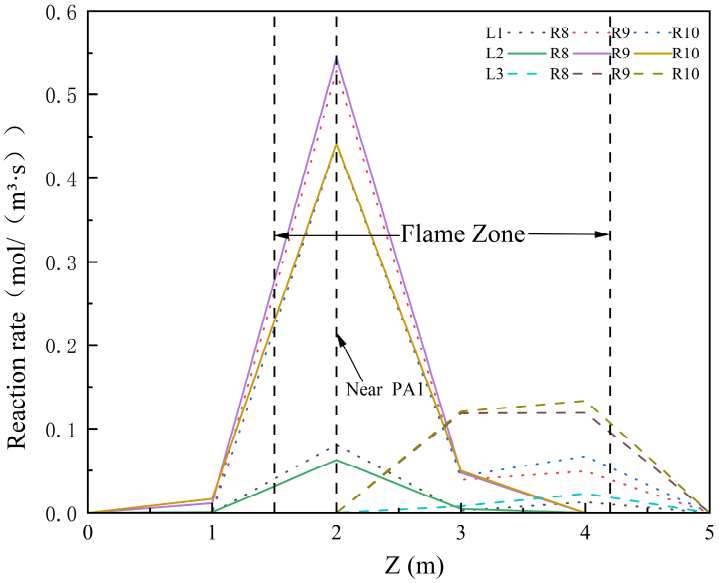

Figure 12. Distribution curves of the reaction rates of ammonia pyrolysis (R8), oxidation (R9), and reduction (R10) along the furnace height under different ammonia positions.

In summary, the three ammonia injection configurations show marked differences in combustion efficiency and pollutant emissions. Case L3, with an excessive injection height, hinders interaction with reducing gases, leading to the highest NO formation, unstable flame structures, and low burnout; therefore, it is unsuitable. In contrast, Cases L1 and L2 perform well across most indicators. Case L2 achieves the highest burnout efficiency, complete CO oxidation, and a stable velocity field, but with relatively high NO emissions due to intensified reactions. Case L1 maintains high burnout efficiency while significantly reducing NO emissions, reflecting an optimal mixing structure and reducing the atmosphere. Overall, L1 and L2 demonstrate the greatest potential and are identified as priority strategies for further optimization.

4.2. Influence of Ammonia Blending Ratio on NO_x Formation and Reduction

Although there are significant differences in the injection position and fuel structure between L1 and L2 ammonia delivery methods, the core goal of this study is to reveal the generation and reduction mechanism of nitrogen oxides under ammonia-coal co-combustion conditions. Among them, the L1 working condition adopts the premixed fuel configuration in the same layer, and ammonia and pulverized coal are injected into the main combustion zone through primary air, forming a combustion mode characterized by synchronous combustion and uniform mixing; while the L2 working condition corresponds to a typical fuel staging (reburning) configuration. Ammonia is injected from the lower layer and forms a “main combustion-reburning-burnout” three-zone structure with the upper main combustion zone, which strengthens the reduction reaction in the reburning stage. In view of the previous systematic analysis of the impact of the ammonia passage position on the flow and combustion characteristics in the furnace, this section further focuses on the NO emission response law under different ammonia doping ratios, and

quantitatively explains the nitrogen oxide control mechanism from the perspective of reburning reaction intensity and free radical conversion. The research results can provide a theoretical basis for optimizing the fuel distribution strategy and denitrification scheme under ammonia-coal co-firing conditions.

4.2.1. The Effect of Ammonia Blending Ratio on NO_x Part at L1 Ammonia Position

Figure 13 illustrates the distribution of NO mass fraction at various ammonia blending ratios. As the ammonia proportion gradually increases, NO formation in the main combustion zone is significantly reduced; the red high-concentration regions in the figure progressively diminish and eventually disappear. This indicates that ammonia addition partially suppresses the formation of both thermal NO and fuel NO. This suppression becomes particularly pronounced when the ammonia blending ratio exceeds 20%, resulting in a substantial decrease in overall NO concentration within the furnace. Analysis shows that at low blending ratios, ammonia tends to participate in NO formation reactions in high-temperature oxidizing environments, whereas at higher blending ratios, its reducing properties dominate, promoting NO reduction and thereby inhibiting its formation. Overall, NO emissions exhibit a "first increase, then decrease" trend as the ammonia blending ratio increases.

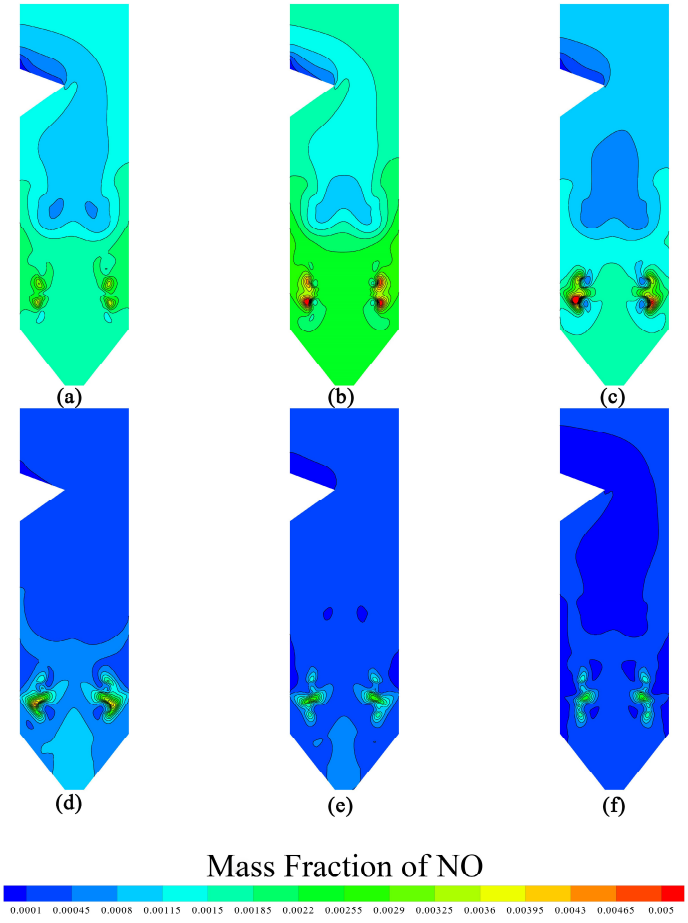

Figure 13. Distribution of longitudinal NO concentration in the furnace under different ammonia blending ratios under the L1 condition, corresponding to (**a**) 5%, (**b**) 10%, (**c**) 15%, (**d**) 20%, (**e**) 25%, and (**f**) 30%.

Figure 14 illustrates the distribution of NO mass fraction at the SA2 cross-section under varying ammonia blending ratios. As the blending ratio increases, a pronounced change in NO generation across the section is observed. Consistent with the trends identified in the

longitudinal contour analysis, the regions of high NO concentration gradually diminish with increasing ammonia proportion. At higher blending ratios, the NO concentration across the entire section decreases significantly. This indicates that the introduction of ammonia effectively suppresses NO formation, particularly when the blending ratio exceeds 20%, at which point the enhanced reducing capability of ammonia dominates the NO reduction process, thereby inhibiting the formation of thermal NO. At low blending ratios, ammonia in a high-temperature oxidizing atmosphere tends to participate in NO formation reactions, resulting in greater NO yield in the main combustion zone—a phenomenon consistent with the elevated NO concentrations observed in the longitudinal distribution plots. As the blending ratio increases, the reducing effect of ammonia becomes progressively stronger, the NO formation region contracts, and at sufficiently high blending ratios, the NO concentration nearly disappears, indicating that ammonia reduction reactions have become the predominant pathway.

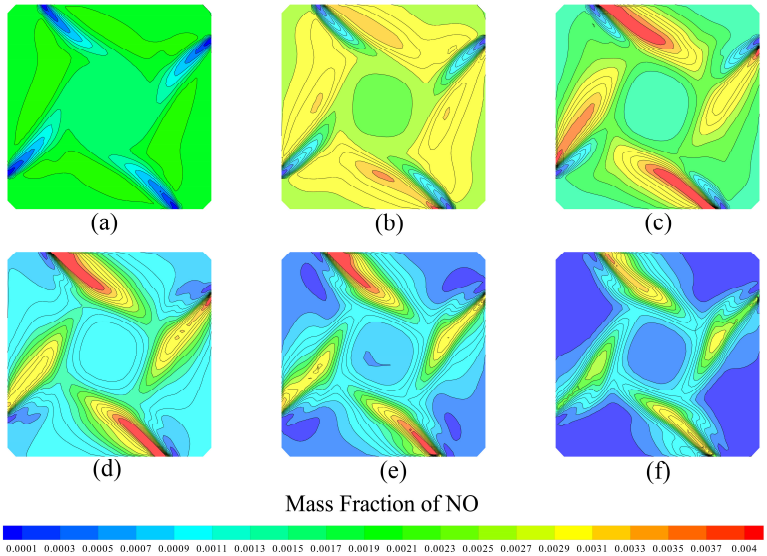

Figure 14. Distribution of NO concentration in the SA2 cross-section under different ammonia blending ratios under the L1 condition, corresponding to (**a**) 5%, (**b**) 10%, (**c**) 15%, (**d**) 20%, (**e**) 25%, and (**f**) 30%.

As shown in Figure 15, under the L1 condition, the flue gas temperature at the furnace outlet initially increases and then decreases with the ammonia blending ratio: 1128.8 K at 5%, peaking at 1130.9 K at 10%, and subsequently declining to 1118.9 K at 30%. When the blending ratio is between 5% and 15%, the outlet NH_3 mole fraction remains on the order of 10^{-19} to 10^{-18}, indicating that ammonia is almost completely consumed within the furnace. However, at a 20% blending ratio, the NH_3 concentration increases markedly, reaching 2.43×10^{-16} and 1.10×10^{-15} at 25% and 30%, respectively, suggesting that high blending ratios hinder complete ammonia conversion and lead to elevated slip. Overall, lower ammonia blending ratios result in higher combustion temperatures and minimal ammonia slip, whereas excessive blending not only lowers the temperature but also significantly increases ammonia emissions. Therefore, the optimal ammonia blending ratio should be maintained within the range of 15% to 20%.

Figure 16a illustrates the longitudinal NO concentration profiles in the furnace under the L1 condition for various ammonia blending ratios. Under pure coal firing, the overall NO emission is relatively low, with a peak of approximately 1520 ppm. As the blending ratio increases to 5% and 10%, NO concentrations rise sharply, reaching a maximum of about 3200 ppm at 10%. This indicates that, at low blending ratios, NH_3 decomposition in the high-temperature oxidizing atmosphere produces reactive radicals such as NH and

NH_2, which react with oxygen radicals, thereby enhancing both thermal and fuel NO formation. When the blending ratio is further increased to 15%, 20%, 25%, and 30%, NO concentrations exhibit a decreasing trend, with the peak dropping to around 750 ppm at 30%, significantly lower than that at 10%. This suggests that, at higher blending ratios, reduction reactions dominate, with NH_x radicals cooperating with reducing gases such as CO to effectively promote NO-to-N_2 conversion. Figure 16b quantitatively depicts the impact of ammonia blending ratio on the outlet NO concentration. In the 0–10% range, the uncorrected NO concentration increases from 424.2 ppm to a peak of 1205.4 ppm, while the oxygen-corrected value rises from 333.8 ppm to 935.4 ppm, both showing a clear upward trend. When the blending ratio exceeds 10%, NO emissions drop sharply; at 30%, the uncorrected and oxygen-corrected NO concentrations are only 181.9 ppm and 142.2 ppm, respectively, representing an approximately 85% reduction from the peak values. These results indicate that, under the present conditions, a blending ratio of 10% represents a critical transition point between NO formation and reduction, with formation dominating at low ratios and reduction prevailing at high ratios, thereby enabling substantial NO suppression.

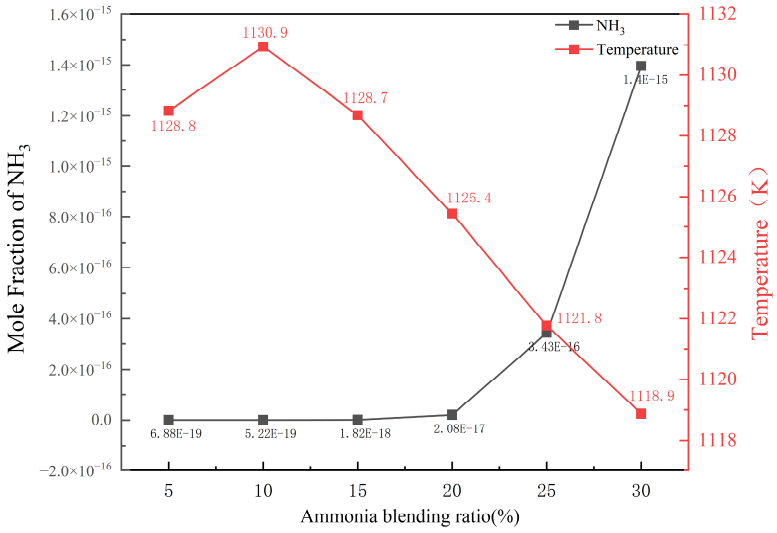

Figure 15. Distribution curves of outlet flue gas temperature and NH_3 mole fraction under different ammonia blending ratios in L1 conditions.

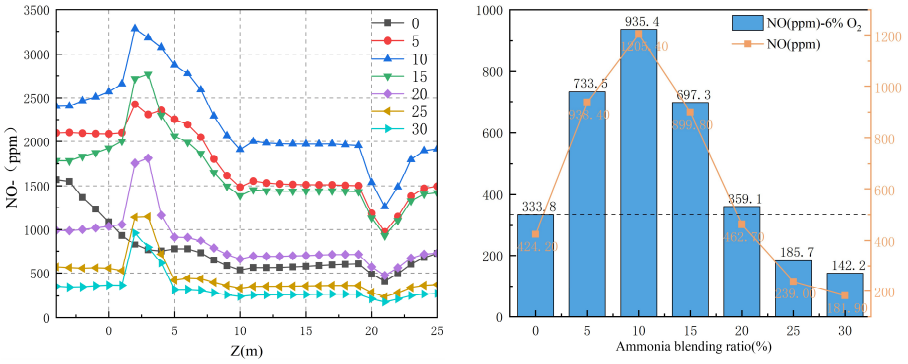

Figure 16. Distribution of NO concentration under different ammonia blending ratios for the L1 operating condition. (**a**) The longitudinal distribution curve of NO concentration in the furnace. (**b**) Distribution of NO concentration at the outlet with the change in ammonia blending ratio.

4.2.2. The Effect of Ammonia Blending Ratio on NO_x Part at L2 Ammonia Position

Figure 17 shows that as the ammonia blending ratio increased from 5% to 30%, the NO concentration initially increased before rapidly declining in the later stages. This indicates that at lower blending ratios, ammonia primarily participates in NO formation, whereas at ratios above 15%, reduction reactions become dominant, significantly weakening NO formation. At a blending ratio of 30%, the NO distribution within the furnace approached a uniformly low level, demonstrating an exceptionally pronounced denitrification effect. This phenomenon confirms that ammonia injection at the L2 position can achieve effective synergy between NO formation and reduction reactions, offering both a high NO_x reduction potential and stable combustion performance.

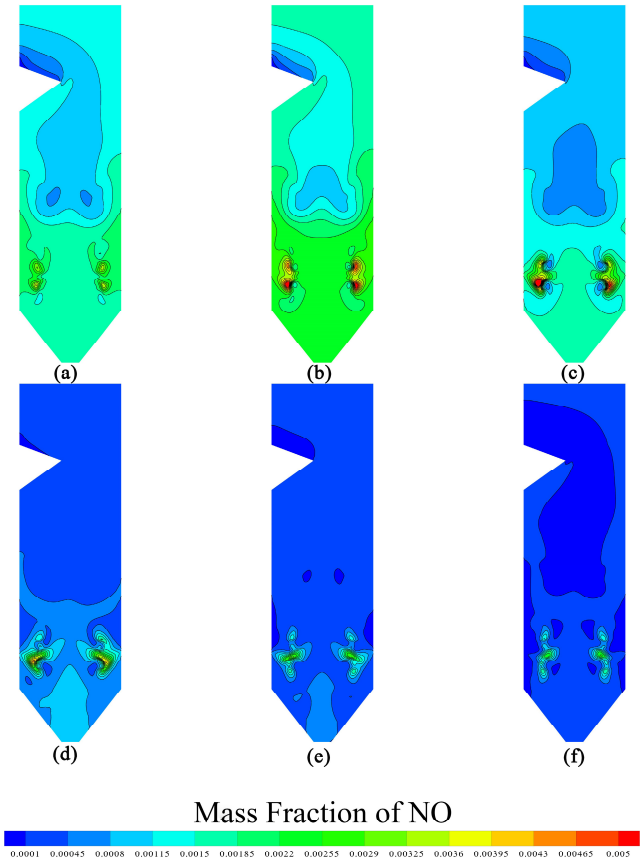

Figure 17. Distribution of longitudinal NO concentration in furnace under different ammonia blending ratios under the L2 condition, corresponding to (**a**) 5%, (**b**) 10%, (**c**) 15%, (**d**) 20%, (**e**) 25%, and (**f**) 30%.

Figure 18 presents the distribution of the NO mass fraction at the SA2 cross-section under different ammonia blending ratios. The results show that within the 5–15% blending range, the NO mass fraction increases significantly, with the central region transitioning from a low-concentration zone to a uniformly high-concentration area, indicating that ammonia predominantly contributes to the NO formation at this stage. When the blending ratio increased to 25% or higher, the NO mass fraction decreased markedly. In particular, at a 30% blending ratio, the NO concentration distribution reverted to a pattern of higher values at the periphery and lower values at the center, reflecting the establishment of a stable NH_x-driven NO reduction zone in the furnace core, thereby achieving a pronounced denitrification effect.

As shown in Figure 19, under the L2 configuration, increasing the ammonia blending ratio from 5% to 30% led to a monotonic decrease in the flue gas outlet temperature, which decreased from 1161.7 K to 1143.4 K. This indicates that ammonia undergoes endothermic decomposition in the high-temperature zone and participates in NO reduction reactions, thereby weakening the overall heat release during combustion. When the ammonia blending ratio is below 25%, the outlet NH_3 mole fraction remained in the range of 10^{-20}–10^{-21}, suggesting that ammonia was almost completely consumed within the furnace and the risk of ammonia slip was negligible. However, when the blending ratio was increased to 30%, the NH_3 mole fraction increased sharply to 5.38×10^{-18}, indicating a clear occurrence of ammonia slip. This finding demonstrates that excessive ammonia supply exceeds the reaction capacity of the furnace, resulting in a reduced combustion temperature and an increased risk of ammonia emissions at the tail end. Overall, maintaining the ammonia blending ratio below 25% is favorable for minimizing temperature losses while avoiding excessive ammonia reduction.

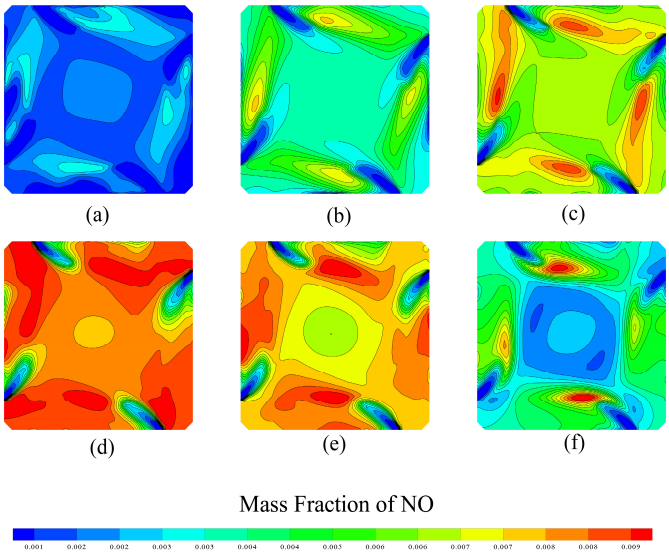

Figure 18. Distribution of NO concentration in SA2 cross-section under different ammonia blending ratios under the L2 condition, corresponding to (**a**) 5%, (**b**) 10%, (**c**) 15%, (**d**) 20%, (**e**) 25%, and (**f**) 30%.

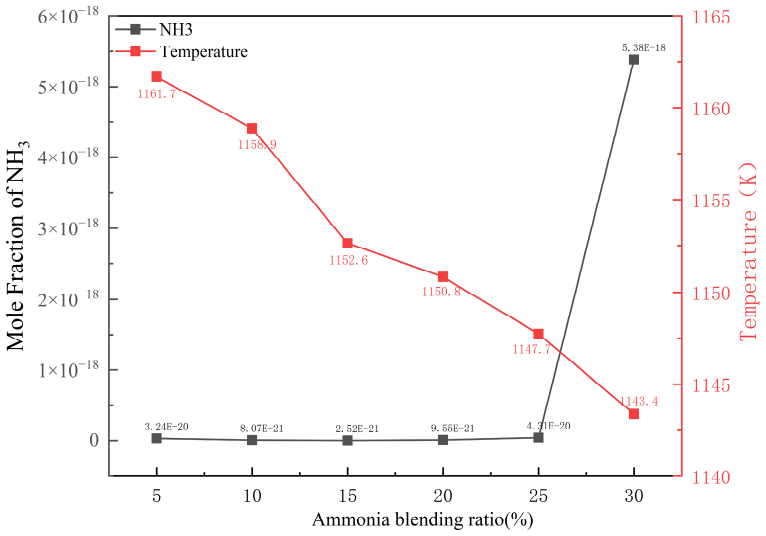

Figure 19. Distribution curves of outlet flue gas temperature and NH_3 mole fraction under different ammonia blending ratios in L2 condition.

As shown in Figure 20a, under pure coal combustion conditions, the NO emission concentration is generally at a low level, and the peak value in the main combustion zone is approximately 1500 ppm. As the ammonia blending ratio increases, the NO concentration increases significantly, reaching the highest peak of about 9000 ppm at a 20% blending ratio, and then gradually decreases. In the L2 working condition, ammonia is injected from the lower layer and forms a typical "three-zone structure" with the upper main combustion zone, namely the main combustion zone, the reburning zone, and the burnout zone. When the ammonia doping ratio is less than 20%, the ammonia in the reburning zone is partially oxidized to generate intermediate free radicals such as NH and NH_2. These species can not only react with O and OH free radicals to promote the generation of NO, but may also form by-products such as N_2O under thermal conditions, resulting in a sharp increase in NO emissions. When the blending ratio is greater than 20%, the concentration of NH_x radicals in the furnace increases significantly, the reaction system changes from oxidation-dominated to reduction-dominated, the reduction path gradually dominates, and the NO generation rate decreases. Figure 20b further confirms this trend. The NO concentration shows a typical "first increase and then decrease" characteristic with the blending ratio. It reaches the peak at 20% blending (2028.97 ppm without correction, 1520.3 ppm after correction), and then drops to about 560.8 ppm and 422.3 ppm at 30%, which is about 72% lower than the peak value. This shows that the L2 ammonia passing mode essentially exhibits the typical staged combustion characteristics of the reburning system: a low proportion of ammonia strengthens the oxidation reaction, and a high proportion of ammonia strengthens the reduction reaction. In general, when the ammonia blending ratio exceeds 20%, the L2 injection configuration enters the effective reburning stage, and the reduction reaction of NO by NH_x radicals dominates, showing significant denitrification potential.

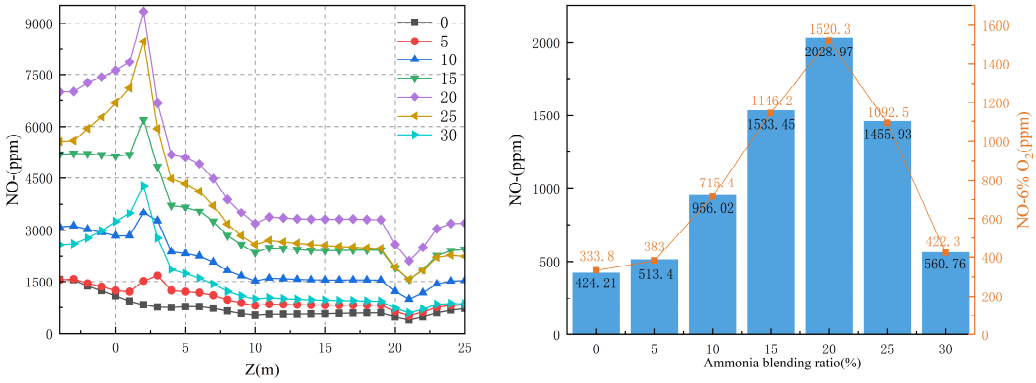

(**a**) (**b**)

Figure 20. Distribution of NO concentration under different ammonia blending ratios for the L2 operating condition. (**a**) The longitudinal distribution curve of NO concentration in the furnace. (**b**) Distribution of NO concentration at the outlet with the change in ammonia blending ratio.

Overall, there are significant differences in the NO emission patterns and control mechanisms between L1 and L2 ammonia delivery methods when the ammonia doping ratio changes. Under the L1 operating condition (same-layer premixed combustion), the NO concentration first increased and then decreased with the ammonia mixing ratio, reaching a peak (about 935 ppm) at 10% mixing, which was about 180% higher than the baseline operating condition, and then dropped rapidly as the ammonia mixing ratio further increased, and dropped to about 142 ppm at 30%, which was about 60% lower than the baseline. At low to medium blending ratios, the outlet NH_3 concentration remains on the order of 10^{-19}–10^{-18}, indicating that ammonia is almost completely involved in the combustion

reaction. The results show that adding an appropriate amount of ammonia can effectively promote the reburn reaction and inhibit the generation of NO, while excessive doping of ammonia will cause local over-reduction and weaken the flame reaction activity and burnout effect. Based on the comprehensive combustion stability and emission reduction performance, the optimal blending range of L1 is 15–20%. Within this range, both NO suppression and combustion efficiency can be taken into consideration.

In comparison, the L2 operating condition is a typical fuel-staged (reburning) configuration. Ammonia is injected from the lower layer to form a staged combustion structure of main combustion zone-reburning zone-burnout zone. NO emissions increase as a whole with the ammonia mixing ratio, reaching a peak (about 2029 ppm) at 20%, which is about six times higher than the baseline operating condition, and then slightly decreases to about 1093 ppm at 30%. This trend reflects the typical phased characteristics of the reburning reaction: When the ammonia doping ratio is less than 20%, ammonia reacts with O and OH radicals in the reburning zone to promote the generation of thermal NO; when the ammonia doping ratio is greater than 20%, the NH_x radical concentration rises and the atmosphere turns to reducing, and NH, N, and other free radicals gradually dominate the NO reduction reaction, reducing emissions. In terms of comprehensive emissions and stability, L2 should avoid the intermediate blending range of 10–20% and prefer a mild reburning strategy of less than 5% or an enhanced reduction strategy of more than 25% to balance denitrification efficiency and combustion stability.

4.3. Identification of NO Formation and Reduction Pathways Under Ammonia Co-Firing and Their Impact on Combustion Performance

By analyzing the furnace temperature field, gas component distribution, and NO_x emission characteristics under different ammonia injection positions and mixing ratios, it is clear that a reasonable ammonia injection strategy can simultaneously improve combustion efficiency and effectively suppress NO generation. However, it is still difficult to reveal the key reaction pathways and free radical reaction mechanisms of ammonia involved in the generation and reduction of NO by relying solely on macroscopic field distribution. Therefore, it is necessary to conduct more in-depth mechanism analysis with the help of fine chemical kinetic models. In order to further clarify the generation and reduction mechanism of NO during the ammonia-coal co-combustion process, CHEMKIN is introduced in this section to combine the macroscopic distribution characteristics obtained by Fluent with the microscopic calculation results at the reaction mechanism level to achieve multi-scale mechanism coupling analysis. Since CHEMKIN uses a zero-dimensional steady-state reactor framework, it is difficult to directly reflect the complex spatial flow structure and differences in ammonia injection positions in the furnace. This study selected the representative L1 configuration as the research object, and fixed the ammonia blending ratio at 15% in the subsequent analysis to focus on exploring the reaction mechanism characteristics under typical co-firing conditions.

4.3.1. Reaction Pathway Analysis

From Figure 21, it can be observed that NO formation primarily originates from the oxidation of solid-phase carbon (CHAR) under oxygen-rich conditions, indicating that unburned carbon particles in high-temperature zones remain the dominant source of NO in the flue gas. In addition, nitrogen atoms reacting with active radicals such as OH and O at elevated temperatures significantly promote NO formation, representing an important pathway that is second only to CHAR oxidation. Moreover, NH radicals can be oxidized to form NO, whereas HNO undergoes thermal decomposition at high temperatures to generate NO, with both species serving as intermediate contributors to NO formation. The thermal decomposition of NO_2 also yields NO, suggesting that NO in the system is

not only continuously generated but can also be regenerated from downstream oxidation products, forming a certain reaction chain. NO reduction is mainly achieved via gas–solid reactions between CHAR and NO, particularly in locally oxygen-deficient zones or regions with high char concentrations, where the reaction rate is elevated. Furthermore, NO can react with OH to form HONO, thereby lowering the instantaneous NO concentration in the atmosphere. HONO, together with intermediate species such as NO_2, participates in the secondary transformation processes of NO.

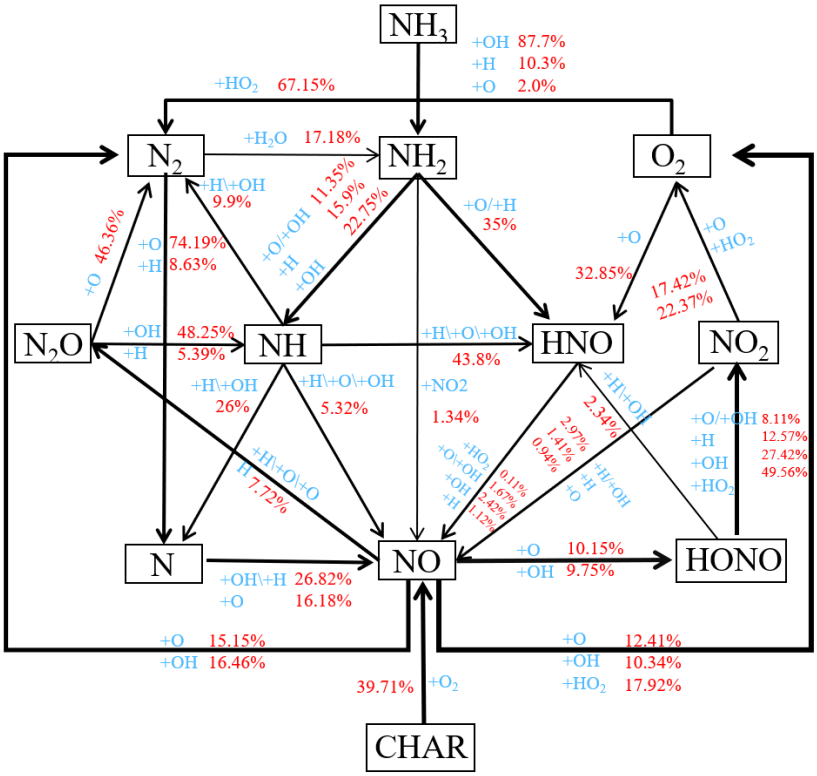

Figure 21. The reduction path of NO formation during ammonia–coal co-combustion in the flame zone.

4.3.2. Analysis of Productivity Rate

It can be seen from Figure 22 that the contribution of different reactions to NO generation and reduction in each region is significantly different. R430 (N + OH→NO + H) and R349 (HNO + OH→NO + H_2O) show positive values in most areas and are the main gas phase channels for NO generation, among which R430 contributes the most. Although R430 has been considered a typical NO generation reaction, this study further reveals its dominance differences in different spatial regions: this reaction is significantly enhanced in the burnout zone, while its effect is weakened in the fuel-rich main combustion zone, indicating that it is closely related to the local redox atmosphere and ammonia circulation position. R14 (CHAR + 208.5O_2→412CO + 5NO) has an enhanced effect in the upper burnout zone, indicating that oxidation of the carbon surface will further promote the formation of NO. On the contrary, R15 (CHAR + NO→CHAR + 0.5N_2 + 0.5O_2), R427 (NH + NO→N_2 + OH), and R432 (N + NO→N_2 + O) all show negative values and are the main NO reduction channels. Among them, R15 contributes the most significantly in the lower region, reflecting the dominant role of heterogeneous reduction. Taken together, the main combustion zone uses R15 and R427 reactions to achieve NO reduction, while the burnout zone causes NO regeneration due to the enhanced oxidation reaction (especially R430 and R14).

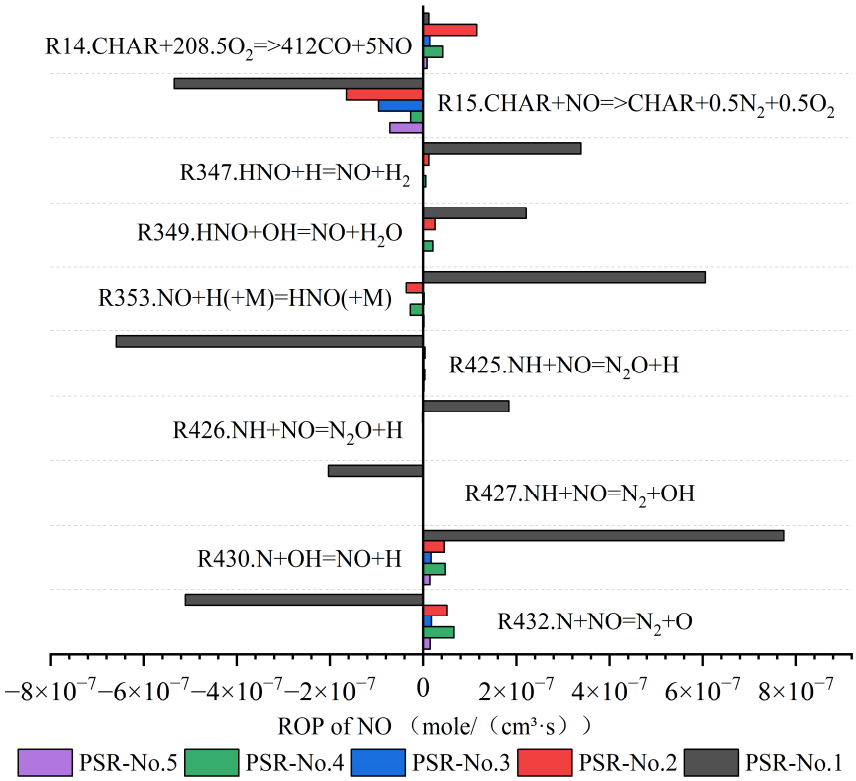

Figure 22. Analysis of NO yield in different regions.

4.3.3. Sensitivity Analysis

It can be seen from Figure 23 that there are significant differences in the effects of different reactions on NO generation and reduction in each reactor area. Overall, R43 shows strong positive sensitivity in all regions and is the main oxidation channel for NO generation; R399 and R419 are also positively sensitive, indicating that HNO, as a key precursor for NO formation, significantly promotes NO generation in an oxidizing atmosphere. In comparison, R427 is negatively sensitive in all regions with larger amplitude, and is the dominant NO reduction reaction in the gas phase system. It is worth noting that R43 shows negative sensitivity in the main combustion zone (reactor 1), but appears slightly positive sensitivity in the upper area, which is not inconsistent with its NO removal channel in the chemical sense. This phenomenon may be due to the local free radical coupling effect: in the highly oxidizing burnout zone, the O atoms generated by R432 can promote oxidation reactions such as R430 and R349, thus showing "apparent positive sensitivity" in steady-state equilibrium. This shows that although this reaction still plays a role in reducing NO locally, there is competition and feedback with other oxidation pathways in the global reaction network, reflecting complex free radical regulation characteristics. In addition, the opposite phase response also has an important influence on NO behavior. R15 shows significant negative sensitivity in the reduction zone and is an important carbon–nitrogen surface reaction for NO reduction, while R14 is positively sensitive in the burnout zone, indicating that the oxidation process of carbon particles in an oxidative atmosphere will actually promote the generation of NO. Comprehensive analysis shows that the NO generation and reduction process in the ammonia-coal co-combustion system is regulated by the coupling of gas-phase free radical reactions and carbon surface reactions, among which R427 and R15 constitute the main reduction channel, while R430 and R14 are key contribution reactions to NO generation.

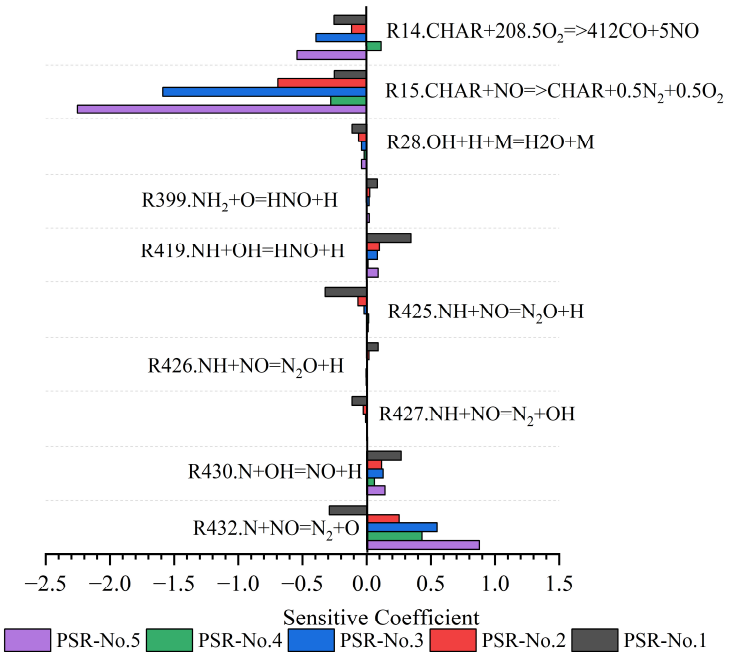

Figure 23. NO sensitivity analysis under different regions.

From Figure 24, it can be observed that the NO concentration decreases significantly in Reactors 2 and 3, confirming the enhanced effect of NH_3 on the NO reduction reactions in both the main flame zone and reduction zone. Meanwhile, the Char concentration progressively decreased across all reaction zones, with a particularly notable reduction in the main combustion and reduction regions, indicating its critical role in promoting NO reduction and sustaining a locally reducing atmosphere. In terms of temperature, although the overall temperature under coal–ammonia co-firing was slightly lower, the main combustion zone maintained a relatively high temperature, which was conducive to sustaining stable combustion reactions. The O_2 content was slightly lower under ammonia co-firing conditions, indicating that the participation of ammonia enhanced the locally reducing atmosphere, thereby favoring NO reduction. The CO distribution results suggest that coal–ammonia co-firing improves burnout efficiency, while the NH_3 concentration is almost completely depleted in the early reaction stage, with no significant residual detected in subsequent reactors, thus avoiding the risk of secondary pollution.

In summary, under ammonia co-firing conditions, NO formation is primarily dominated by the oxidation of CHAR in oxygen-rich atmospheres and high-temperature oxidation reactions between nitrogen atoms and reactive radicals such as OH and O, among which R430 (N + OH → NO + H) is identified as the most critical reaction pathway. HNO, an intermediate species, exhibits sustained transformation potential within the NO formation chain. NO reduction mainly relies on the gas–solid phase reduction reaction between CHAR and NO (R15), whereas NH radicals significantly suppress NO via multiple pathways (e.g., R425, R427), reacting with NO to form N_2 or N_2O in the flame and reduction zones. The spatial distribution of NO concentrations, together with the trend of char consumption across reaction zones, further confirmed that NO formation was strongly influenced by the competition between the oxidation and reduction pathways. The introduction of ammonia enhanced the radical activity and strengthened the locally reducing atmosphere, effectively promoting NO reduction while improving burnout efficiency. The absence of residual ammonia indicates that coal–ammonia co-firing has both strong denitrification potential and favorable combustion performance.

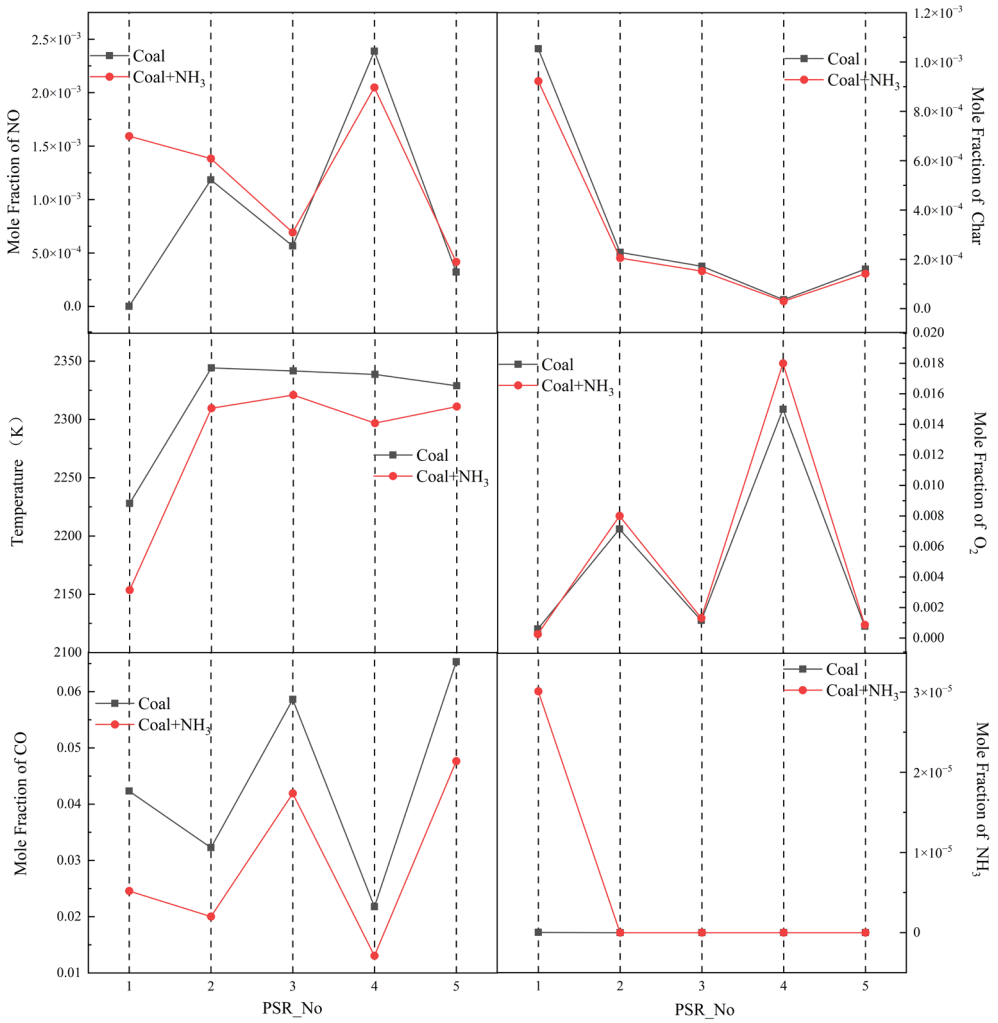

Figure 24. Comparison of temperature and mole fraction distribution of main gas components (NO, Char, CO, O_2, NH_3) in different reactors (PSR No. 1–5) under the condition of pure coal and coal-ammonia co-combustion.

5. Conclusions

Taking a 125 MW square tangential pulverized coal boiler as the research object, a numerical model was established based on Fluent and Chemkin to conduct a multi-scale coupling analysis of NO_x emissions and combustion performance under ammonia-coal mixed combustion conditions. This study focuses on the synergistic effects of ammonia injection strategy, ammonia doping ratio, NO reaction pathway, and sensitivity on combustion and NO_x emission performance. The main conclusions are as follows.

1. The ammonia injection position has a significant impact on the combustion structure and NO emissions. In the L1 case, ammonia and pulverized coal are co-injected from the upper port, which can establish the flame early, maintain a continuous flame structure, and achieve lower NO emissions. In the case of L2, ammonia is injected separately from the lower port to achieve effective layered coupling with the pulverized coal injected from the upper port. This configuration exhibits the highest combustion efficiency and flame extension but results in strong NO formation at intermediate mixing ratios. In the case of L3, ammonia is injected independently from the upper port, causing the ammonia injection area to be misaligned with the main combustion area, causing vertical recirculation in the flow field, resulting in unstable flame structure and the worst NO control effect. These results show that L1 is more

conducive to inhibiting NO formation, L2 is more suitable for synergistic burnout and reduction reactions, and L3 is not conducive to efficient tissue combustion.

2. The two ammonia passing methods, L1 and L2, show significant differences when the blending ratio changes: In L1 (same-layer premixed combustion), NO emissions show a "first rise and then drop" trend with the blending ratio. An appropriate amount of ammonia can strengthen the reburning reaction and effectively inhibit the generation of NO, while excessive ammonia will lead to a decrease in combustion intensity due to local over-reduction. Taking into account emission reduction and combustion performance, the optimal blending range of L1 is 15–20%. The L2 operating condition (fuel staged configuration) shows typical reburning stage characteristics. NO reaches a peak at a medium blending ratio (about 20%). At low proportions, thermal oxidation is dominant. At high proportions, NH_x radicals dominate the reduction reaction, significantly reducing emissions. In general, L1 is conducive to stable combustion and suppressing NO generation, while L2 can achieve enhanced reduction at high blending ratios. The intermediate blending interval of 10–20% should be avoided to prevent higher NO generation.
3. Microscopic mechanism analysis reveals key NO control pathways and regional characteristics. Chemkin-based ROP and sensitivity analysis showed that N + OH → NO + H is the main NO formation pathway, while CHAR + NO and NH + NO reactions constitute the main NO reduction mechanism. In the flame and reduction zone, the NO concentration is significantly reduced, the degree of coke participation in the reaction continues to increase, and the NH_3 concentration is rapidly depleted, confirming the establishment of a medium–high temperature reduction environment and effectively realizing the collaborative optimization of NO reduction and combustion performance.
4. There are certain simplifications and sources of error in the model. In order to balance calculation efficiency and convergence stability, the combustion process assumes that pulverized coal devolatilizes instantaneously after entering the furnace, and that volatile matter and oxidants are completely mixed and in a thermodynamic equilibrium state. At the same time, the effects of ash heat transfer and some heterogeneous reactions are ignored, so that the reaction in the furnace can be approximately regarded as an ideal continuous flow system. Turbulent combustion, radiation heat transfer, and chemical reaction mechanisms are also simplified, and small-scale turbulent fluctuations and transient non-uniform effects are not fully analyzed. Although the simulation results can generally reflect the changing patterns under different ammonia delivery methods and blending ratios, there may still be deviations in the local temperature distribution and NO peak value. Follow-up research can further improve the accuracy and physical completeness of the model by introducing unsteady turbulence models, fine meshing, and experimental comparisons.

Author Contributions: Y.X. (Yuhang Xiao): Writing—original draft, Validation, Formal analysis, Investigation, Writing—Review and Editing; J.C.: Conceptualization, Methodology, Writing—original draft, Project administration, Funding acquisition; H.P.: Software, Data curation; L.Z.: Formal analysis; B.X.: Supervision; X.Y.: Software, Data curation; H.Z.: Investigation, Resources; S.Y.: Validation, Data curation, Funding acquisition; Y.Z.: Formal analysis; M.W.: Supervision; Y.X. (Youning Xu): Methodology, Supervision. All authors have read and agreed to the published version of the manuscript.

Funding: Project of Xinjiang Coal Clean Combustion and Energy Storage Research and Development Center Co., Ltd. (No.: XJKT2024-03), Department of Science and Technology of Liaoning Province (No.: 2023JH2/101700257 and 2023JH2/101700256).

Data Availability Statement: The original contributions presented in this study are included in the article. Further inquiries can be directed to the corresponding author.

Conflicts of Interest: Authors Liang Zhu, Benchuan Xu were employed by the company Xinjiang Saier Shan Municipal Engineering Co., Ltd. The remaining authors declare that the research was conducted in the absence of any commercial or financial relationships that could be construed as a potential conflict of interest.

Abbreviations

CFD	Computational Fluid Dynamics
CHEMKIN	Chemical Kinetics Simulation Software
PA	Primary Air
SA	Secondary Air
OFA	Overfire Air
SOFA	Separated Overfire Air
PSR	Perfectly Stirred Reactor
PFR	Plug Flow Reactor
DPM	Discrete Phase Model
RANS	Reynolds-Averaged Navier–Stokes
EDM	Eddy Dissipation Model
WSGGM	Weighted Sum of Gray Gases Model
ROP	Rate of Production
FLASHCHAIN	A macromolecular coal pyrolysis model

References

1. Sun, F.; Ji, J.; Zeng, G.; Li, J.; Wei, G. Employment of molten salt thermal energy storage coupled to coal-fired power unit for power grid peak shaving: A thermodynamic study. *J. Energy Storage* **2025**, *131*, 117503. [CrossRef]
2. Lee, B.H.; Bae, Y.H.; Cho, S.H.; Kim, G.M.; Jeon, C.H. Comprehensive technical review for fundamental characteristics and application of NH_3 co-firing with coal. *Chem. Eng. J.* **2023**, *474*, 145587. [CrossRef]
3. Sun, W.; Lin, Q.; Li, H.; Fang, S.; Chen, Y.; Cheng, Y.; Ya, H.; Feng, H. Simulation study on coal and ammonia co-firing in a tangential firing boiler under different ammonia injection methods. *Sci. Rep.* **2025**, *15*, 15768. [CrossRef]
4. Lin, Q.; Sun, W.; Li, H.; Liu, Y.; Chen, Y.; Liu, C.; Jiang, Y.; Cheng, Y.; Ma, N.; Ya, H.; et al. Experimental study on ammonia co-firing with coal for carbon reduction in the boiler of a 300-MW coal-fired power station. *Engineering* **2024**, *40*, 247–259. [CrossRef]
5. Tamura, M.; Gotou, T.; Ishii, H.; Riechelmann, D. Experimental investigation of ammonia combustion in a bench scale 1.2 MW-thermal pulverised coal firing furnace. *Appl. Energy* **2020**, *277*, 115580. [CrossRef]
6. Pak, S.J.; Im, H.T.; Kim, S.J.; Kang, B.G.; Lee, Y.G.; Yu, Y.H.; Ahn, T.I.; Lee, K.; Mun, T.Y. Simultaneous reduction of NO and N_2O via NH_3 injection strategies and fuel-staging during NH_3 co-firing with coal in a pilot scale circulating fluidized bed system. *Appl. Therm. Eng.* **2025**, *2015*, 127589. [CrossRef]
7. Tan, J.; He, Y.; Zhu, R.; Zhu, Y.; Wang, Z. Experimental study on co-firing characteristics of ammonia with pulverized coal in a staged combustion drop tube furnace. *Proc. Combust. Inst.* **2023**, *39*, 3217–3225. [CrossRef]
8. Mathaba, M. Effect of combustion temperature on the unburnt carbon during ammonia co-firing with coal combustion. *Sci. Rep.* **2024**, *14*, 22153. [CrossRef]
9. Wang, Y.; He, Y.; Weng, W.; Wang, Z. Numerical simulation of ammonia combustion with coal in a 135MW tangentially fired boiler. *Fuel* **2024**, *370*, 14. [CrossRef]
10. Wu, X.; Hu, F.; Ding, C.; Yang, Y.; Yang, C.; Liao, H.; Lu, K.; Li, B.; Liu, T.; Liu, C.; et al. Progress in numerical simulations and fundamental characteristics of pulverized coal co-firing with ammonia. *Int. J. Hydrogen Energy* **2024**, *82*, 740–758. [CrossRef]
11. Cardoso, J.S.; Silva, V.; Eusébio, D.; Tarelho, L.A.; Hall, M.J.; Dana, A.G. Numerical modelling of ammonia-coal co-firing in a pilot-scale fluidized bed reactor: Influence of ammonia addition for emissions control. *Energy Convers. Manag.* **2022**, *254*, 115226. [CrossRef]
12. Liu, M.; Chen, S.; Zhu, H.; Zhou, Z.; Xu, J. Numerical investigation of ammonia/coal co-combustion in a low NOx swirl burner. *Energy* **2023**, *282*, 128358. [CrossRef]
13. Wang, S.L. Ammonia–Coal Co-Firing Effects on the Operational Performance of a 600 MW Supercritical Pulverized Coal Boiler. Master's Thesis, Southeast University, Nanjing, China, 2023. [CrossRef]

14. Ma, L.; Fang, Q.Y.; Zhang, C.; Chen, C.; Wang, X. Pulverized Coal Combustion Coupled with Ammonia under Deep Air-Staged Conditions and NO Formation Characteristics. *Clean Coal Technol.* **2022**, *28*, 201–213. [CrossRef]
15. Jin, W.; Si, F.; Cao, Y.; Yu, C.; Wang, J. Numerical research on ammonia-coal co-firing in a 1050 MW coal-fired utility boiler under ultra-low load: Effects of ammonia ratio and air staging condition. *Appl. Therm. Eng.* **2023**, *233*, 121100. [CrossRef]
16. Kim, S.J.; Pak, S.J.; Jo, S.H.; Lee, H.; Yoon, S.J.; Ra, H.W.; Yoon, S.M.; Li, D.; Lee, K.; Mun, T.Y. Combustion characteristics on ammonia injection velocity and positions for ammonia co-firing with coal in a pilot-scale circulating fluidized bed combustor. *Appl. Therm. Eng.* **2024**, *257*, 124338. [CrossRef]
17. Wei, D.; Zhang, Z.; Wu, L.; Wang, T.; Sun, B. Ammonia blend ratio impact on combustion characteristics and NOx emissions during co-firing with sludge and coal in a utility boiler. *Energy* **2023**, *283*, 129220. [CrossRef]
18. Zhang, X.; Gu, X.; Yu, J.; Ni, Y.; Lin, R.; Wang, X.; Feng, H. Combustion characteristics and nitrogen conversion mechanism in ammonia/coal Co-firing process. *Int. J. Hydrogen Energy* **2024**, *69*, 317–330. [CrossRef]
19. Su, X.; Ma, L.; Yao, B.; Liao, W.; Zheng, Y.; Miao, M.; Fang, Q.; Chen, G.; Yang, W. High-efficiency combustion and low-nitrogen emission of coal-fired boiler based on synergistic optimization of swirl burner structure and air-staged technology. *Fuel* **2025**, *388*, 134352. [CrossRef]
20. Cheng, P. Two-dimensional radiating gas flow by a moment method. *AIAA J.* **1964**, *2*, 1662–1664. [CrossRef]
21. Howell, J.R.; Mengüç, M.P.; Daun, K.; Siegel, R. *Thermal Radiation Heat Transfer*; CRC Press: Boca Raton, FL, USA, 2020. [CrossRef]
22. Wang, Y.; Zhou, Y. Numerical optimization of the influence of multiple deep air-staged combustion on the NOx emission in an opposed firing utility boiler using lean coal. *Fuel* **2020**, *269*, 116996. [CrossRef]
23. Langmuir, I. The adsorption of gases on plane surfaces of glass, mica and platinum. *J. Am. Chem. Soc.* **1918**, *40*, 1361–1403. [CrossRef]
24. Ma, Z.Y.; Zhang, X.Y.; Wen, H.N.; Liu, W.; Wang, Z.; Yu, B. Numerical Simulation and Experimental Study on Ammonia–Coal Co-Firing in a 4 MW Boiler. *Therm. Power Gener.* **2025**, *54*, 64–72. [CrossRef]
25. Lyu, Q.; Wang, R.; Du, Y.; Liu, Y. Numerical study on coal/ammonia co-firing in a 600 MW utility boiler. *Int. J. Hydrogen Energy* **2023**, *48*, 17293–17310. [CrossRef]
26. Annamalai, K.; Puri, I.K. *Combustion Science and Engineering*; CRC Press: Boca Raton, FL, USA, 2006. [CrossRef]
27. Field, M.A. Rate of combustion of size-graded fractions of char from a low-rank coal between 1200 K and 2000 K. *Combust. Flame* **1969**, *13*, 237–252. [CrossRef]
28. Pratt, D.T.; Smoot, L.; Pratt, D. *Pulverized Coal Combustion and Gasification*; Springer: Berlin, Germany, 1979. [CrossRef]
29. Jones, W.P.; Lindstedt, R.P. Global reaction schemes for hydrocarbon combustion. *Combust. Flame* **1988**, *73*, 233–249. [CrossRef]
30. Kim, J.P.; Schnell, U.; Scheffknecht, G. Comparison of different global reaction mechanisms for MILD combustion of natural gas. *Combust. Sci. Technol.* **2008**, *180*, 565–592. [CrossRef]
31. Andersen, J.; Rasmussen, C.L.; Giselsson, T.; Glarborg, P. Global combustion mechanisms for use in CFD modeling under oxy-fuel conditions. *Energy Fuels* **2009**, *23*, 1379–1389. [CrossRef]
32. Monnery, W.D.; Hawboldt, K.A.; Pollock, A.E.; Svrcek, W.Y. Ammonia pyrolysis and oxidation in the Claus furnace. *Ind. Eng. Chem. Res.* **2001**, *40*, 144–151. [CrossRef]
33. Brouwer, J.; Heap, M.P.; Pershing, D.W.; Smith, P.J. A model for prediction of selective noncatalytic reduction of nitrogen oxides by ammonia, urea, and cyanuric acid with mixing limitations in the presence of CO. *Symp. (Int.) Oncombustion* **1996**, *26*, 2117–2124. [CrossRef]
34. Hashemi, H.; Hansen, S.; Toftegaard, M.B.; Pedersen, K.H.; Jensen, A.D.; Dam-Johansen, K.; Glarborg, P. A model for nitrogen chemistry in oxy-fuel combustion of pulverized coal. *Energy Fuels* **2011**, *25*, 4280–4289. [CrossRef]
35. Williams, A. *Combustion and Gasification of Coal*; Routledge: Milton Park, UK, 2018. [CrossRef]
36. Ma, P.; Huang, Q.; Wu, Z.; Lyu, J.; Li, S. Optical diagnostics on coal ignition and gas-phase combustion in co-firing ammonia with pulverized coal on a two-stage flat flame burner. *Proc. Combust. Inst.* **2023**, *39*, 3457–3466. [CrossRef]
37. Dai, L.; Wang, C.A.; Hou, Y.; Ma, G.; Chen, Y.; Hurera, A.; Zhou, L.; Che, D. Chemical kinetics simulation on nitrogen migration characteristics during co-combustion of ammonia and coal under deeply fuel-air multistage conditions. *Fuel* **2024**, *376*, 132726. [CrossRef]
38. Niksa, S.; Kerstein, A.R. FLASHCHAIN theory for rapid coal devolatilization kinetics. 1. Formulation. *Energy Fuels* **1991**, *5*, 647–665. [CrossRef]
39. Ishihara, S.; Zhang, J.; Ito, T. Numerical calculation with detailed chemistry of effect of ammonia co-firing on NO emissions in a coal-fired boiler. *Fuel* **2020**, *266*, 116924. [CrossRef]
40. Ding, X.; Li, W.; Liu, P.; Kang, Z. Numerical calculation on combustion process and NO transformation behavior in a coal-fired boiler blended ammonia: Effects of the injection position and blending ratio. *Int. J. Hydrogen Energy* **2023**, *48*, 29771–29785. [CrossRef]

41. Kim, S.J.; Park, S.J.; Jo, S.H.; Lee, H.; Yoon, S.J.; Moon, J.H.; Ra, H.W.; Yoon, S.M.; Lee, J.G.; Mun, T.Y. Effects of ammonia co-firing ratios and injection positions in the coal–ammonia co-firing process in a circulating fluidized bed combustion test rig. *Energy* **2023**, *282*, 128953. [CrossRef]
42. Wang, X.; Fan, W.; Chen, J.; Zhang, H. Experimental study and kinetic analysis of NO emission characteristics in ammonia/coal co-firing process with different ammonia injection methods. *J. Energy Inst.* **2024**, *114*, 101609. [CrossRef]

Disclaimer/Publisher's Note: The statements, opinions and data contained in all publications are solely those of the individual author(s) and contributor(s) and not of MDPI and/or the editor(s). MDPI and/or the editor(s) disclaim responsibility for any injury to people or property resulting from any ideas, methods, instructions or products referred to in the content.